Journal of Physics and Chemistry of Solids 191 (2024) 112033

Contents lists available at ScienceDirect

Journal of Physics and Chemistry of Solids

journal homepage: www.elsevier.com/locate/jpcs

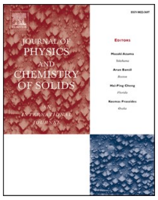

Improving photocatalytic efficiency: Harnessing the importance of Ag@HfO$_2$ core-shell nanostructures

Adem Kocyigit [a], Erman Erdogan [a], Nurtac Canpolat [b], Sakir Aydogan [c], Mehmet Yilmaz [d,e,*]

[a] *Department of Electronics and Automation, Vocational High School, Bilecik Seyh Edebali University, 11100, Bilecik, Turkey*
[b] *Department of Chemistry, K.K. Education Faculty, Ataturk University, 25240, Erzurum, Turkey*
[c] *Department of Physics, Science Faculty, Ataturk University, 25240, Erzurum, Turkey*
[d] *Department of Science Teaching, K.K. Education Faculty, Ataturk University, 25240, Erzurum, Turkey*
[e] *Advanced Materials Research Laboratory, Department of Nanoscience and Nanoengineering, Graduate School of Natural and Applied Sciences, Ataturk University, 25240, Erzurum, Turkey*

ARTICLE INFO

Keywords:
Photocatalysis
Dye degradation
HfO$_2$ shell layers
Ag nanoparticles
Ag@HfO$_2$ core-shell nanostructures

ABSTRACT

Pollution of fresh water has resulted from waste generated by agricultural and industrial activities. The pollutants need to be removed from water owing to the growing demand for drinking water due to an increase in the population. Hence, the effective treatment of synthetic dyes and their release into the environment is crucial. In this study, Ag@HfO$_2$ core-shell nanostructures were synthesized and presented as a new catalyst for removing cationic dyes - such as rhodamine B (RhB), methylene blue (MB), and direct red-23 (DR-23) - from wastewater. X-ray diffractometry (XRD), transmission electron microscopy (TEM), X-ray photoelectron spectroscopy (XPS), UV–Vis, and photoluminescence (PL) spectroscopies were employed to verify the synthesis success of Ag@HfO$_2$ core-shell nanostructures in this study. The Ag@HfO$_2$ core-shell nanostructures' effectiveness for photodegradation were tested by removing dyes associated with photo-catalytic measurements with high efficiency in both the UV and visible regions. The results are expected to contribute towards solving an environmental health issue deemed critical.

1. Introduction

The potential for a long-term threat to the wetland and terrestrial ecosystems from the continuous direct discharge of wastes from agricultural and industrial activities intensified by population growth into natural river beds raises concerns both in developed countries and in water-scarce regions [1]. Hundreds of organic pollutants contaminate in wastewater, and dyes are considered a priority among wastewater pollutants [2]. In general, dyes are divided into two main groups natural dyes and synthetic dyes. While natural dyes are obtained from animal or vegetable substances without any chemical treatment, synthetic dyes are produced from organic molecules [3]. Since chemical processes are involved in the synthesis, processing, and use of synthetic dyes, these dyes have the potential to pose environmental problems [4]. Among the anionic and cationic dyes included in the scope of synthetic dyes, cationic dyes are more harmful to the environment. However, these dyes constitute the main component of the organic content of industrial wastewater [5]. Thus, wastewater generation and treatment are called among the biggest problems in terms of health and the environment today [6]. It is important to search for new, economical, and efficient methods to remove organic pollutants from water. In general, methods for the treatment of dye-containing wastewater are considered in two main groups. The first is chemical or physical dye removal methods, which refer to the process called decolorization, and the other is biodegradation [7]. It can be mentioned that there is photo-catalytic technology, which has much more advantages than the methods mentioned above. Today, heteroatom doping, heterojunction formation, morphology modification, hybridization with cocatalysts, and the use of carbon materials are among the strategies used to improve photo-catalytic performance, in addition to the design of different materials for photo-catalysts [8,9].

Noble metal nanocrystals (especially silver) have been shown to have significant potential for visible light harvesting in the photo-catalytic process due to their specific surface plasmon resonance (SPR)

---

* Corresponding author. Department of Science Teaching, K.K. Education Faculty, Ataturk University, 25240, Erzurum, Turkey.
E-mail addresses: adem.kocyigit@bilecik.edu.tr (A. Kocyigit), erman.erdogan@bilecik.edu.tr (E. Erdogan), nurtac@atauni.edu.tr (N. Canpolat), saydogan@atauni.edu.tr (S. Aydogan), mehmetyilmaz@atauni.edu.tr (M. Yilmaz).

https://doi.org/10.1016/j.jpcs.2024.112033
Received 19 February 2024; Received in revised form 23 March 2024; Accepted 7 April 2024

Table 1
Properties of chemicals used in Ag NPs and Ag@HfO$_2$ core-shell NPs synthesis.

	$AgNO_3$	$HfCl_4$	$HOC(COONa)(CH_2COONa)_2 \cdot 2H_2O$	CH_3OH	NaOH
IUPAC name	Silver nitrate	tetrachlorohafnium	trisodium; 2-hydroxy propane-1,2,3-tricarboxylate; dihydrate	Methanol	sodium; hydroxide
Molecular weight (g/mol)	169.87	320.29	294.10	32.04	39.99
Chemical Structure	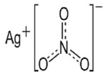	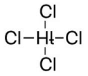	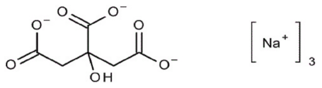	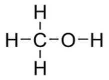	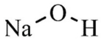
Appearance	White Solid	White Solid	White Solid	Colorless	White Solid
Density (g/cm^3)	4.35	3.89	0.6	0.792	2.13

Table 2
Chemicals used in photo-catalytic activity measurements.

	$C_{28}H_{31}C_lN_2O_3$	$C_{16}H_{18}C_lN_3S$	$C_{35}H_{27}N_7O_{10}S_2$
IUPAC name	[9-(2-carboxyphenyl)-6-diethylamino-3-xanthenylidene]-diethylammonium chloride	3,7-bis(Dimethylamino)-phenothiazin-5-ium chloride	7-[[6-[(4-acetamidophenyl)diazenyl]-5-hydroxy-7-sulfonaphthalen-2-yl] carbamoylamino]-4-hydroxy-3-phenyldiazenylnaphthalene-2-sulfonic acid
Name	Rhodamine B	Methylene blue	Direct-red 23
Molecular weight (g/mol)	479.02	319.85	813.72
Chemical Structure	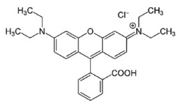	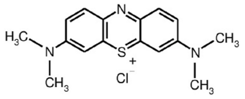	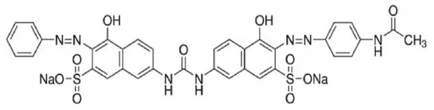
Appearance	Green crystals or reddish-purple powder	Blue powder	Purple powder

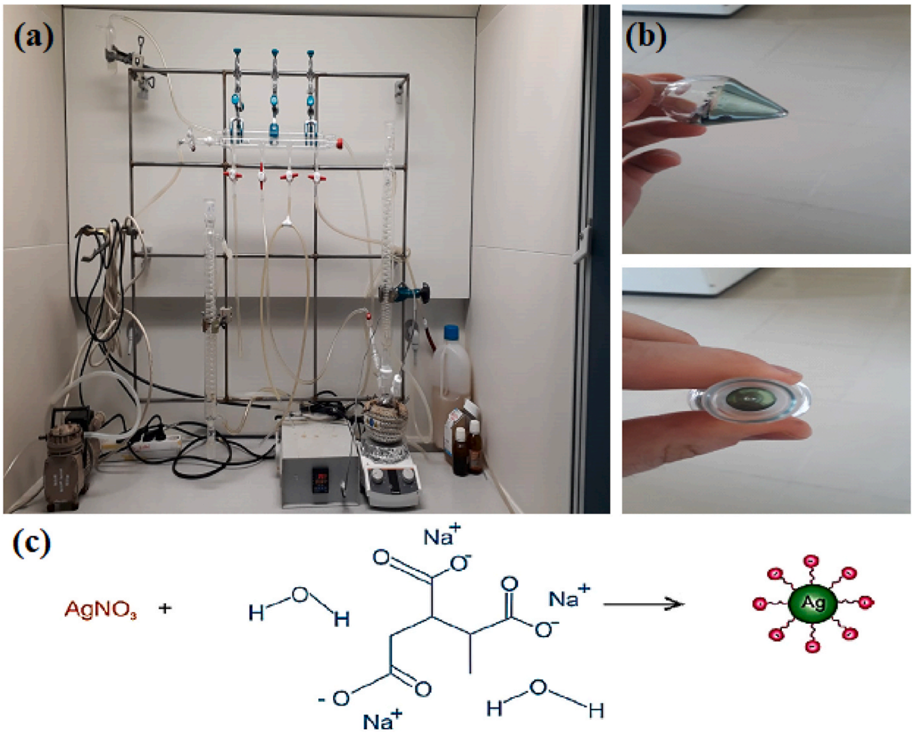

Fig. 1. a) System used in the synthesis of Ag nanoparticles, b) demonstration of the formation of the produced Ag nanoparticles and c) obtaining Ag nanoparticles from AgNO$_3$ [20].

properties [10]. Since the effect of core-shell nanostructures on factors that directly affect photo-catalytic performance, such as rapid photo-generated charge migration, can be controlled by the general architecture of the core-shell structure, it has an important potential to increase clean water from organic impurities. Metal-semiconductor core-shell nanostructured photo-catalysts offer several advantages. The integration of plasmonic metals and semiconductors in hybrid nanostructures enables the combination of their respective functions in a single nano-system, facilitating the synergistic coupling between plasmon and exciton, which in turn enhances the harvesting of sunlight and its

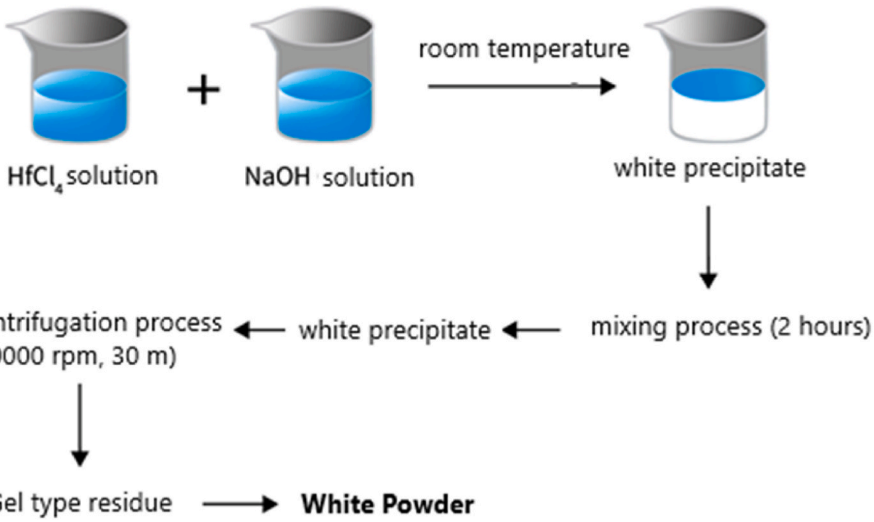

Fig. 2. The synthesizing procedure of HfO_2 shell layers.

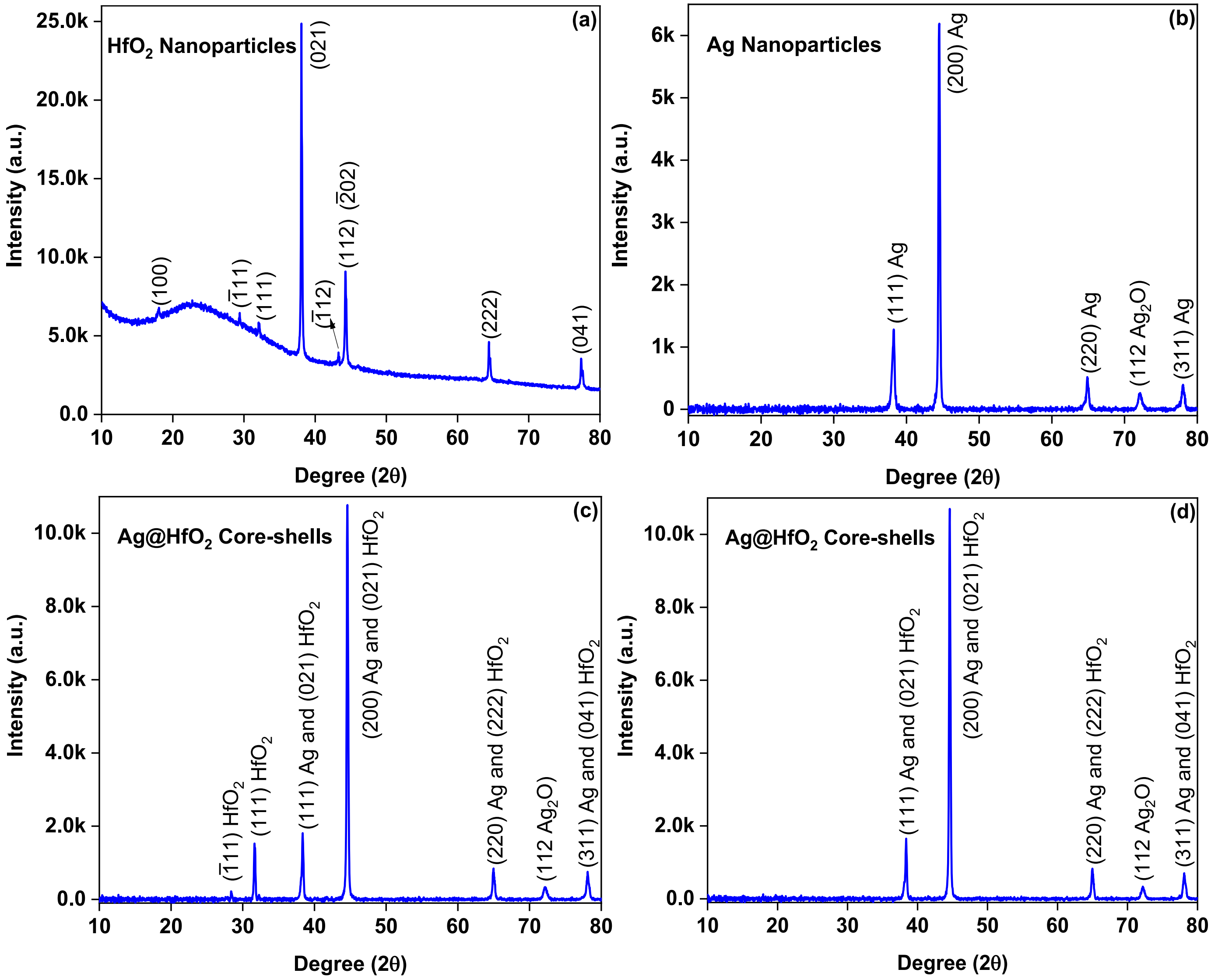

Figure 3. XRD diffraction patterns of a) HfO_2 shell layers, b) Ag nanoparticles, c) Ag@HfO_2-1, and d) Ag@HfO_2-2 core-shell structures.

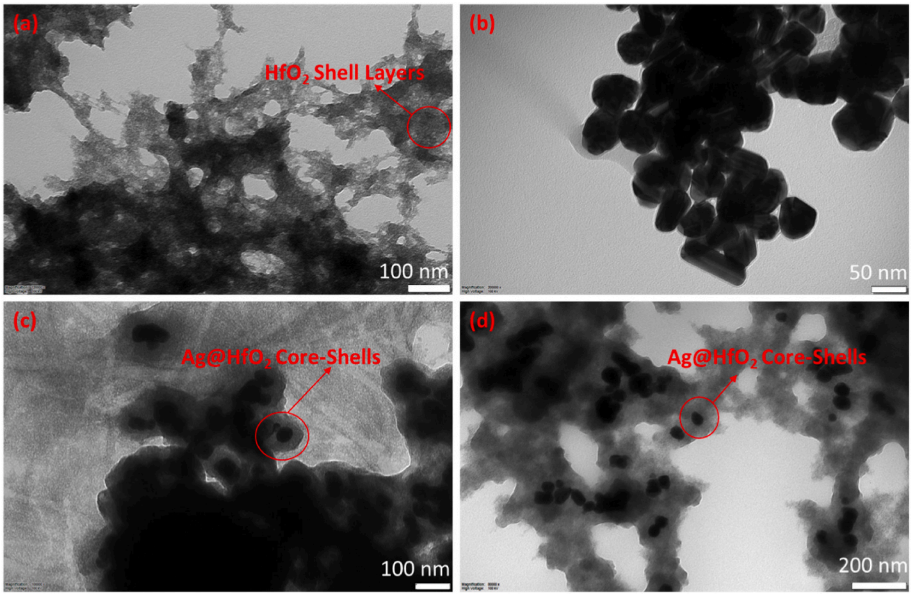

Fig. 4. TEM images of a) HfO_2 shell layers, b) Ag nanoparticles, c) Ag@HfO_2-1, and d) Ag@HfO_2-2 core-shell structures.

conversion into clean energy [11,12]. Nanoparticles of metal-semiconductor core-shell structures such as Ag@SiO_2 NPs and Ag@TiO_2 NPs, have been widely used in micro-nano optoelectronic devices [13,14]. Furthermore, since solar energy is by far the largest available energy source in the world, it is important to devise various strategies to improve the photo-catalytic activity of wide-band gap semiconductors under visible light. In this context, research on zirconium oxide (ZrO_2)-based photo-catalysts has increased recently. Although HfO_2 is similar in crystal structure to ZrO_2, specifically, the presence of a greater electron density concentration on the oxygen atoms of HfO_2 than ZrO_2 makes the electronic structure of HfO_2 different from ZrO_2 [15,16]. This provides an advantageous for photo-catalytic applications for HfO_2 due to trapping of photogenerated electrons especially in UV region [17]. HfO_2 can be used as shell format to capture more charge carriers on the surface for photodegradation of pollutants. Furthermore, it can provide to adjust the SPR of Ag by changing shell thickness [18].

In this study, Ag@HfO_2 core-shell spherical nanostructures at different shell thicknesses were synthesized by a high-temperature reduction technique. The characterization of the Ag@HfO_2 core-shell structures was carried out by various instruments. The investigation of photo-catalytic performance for degradation of various dyes was tested in UV and visible regions.

2. Experimental

2.1. Chemical materials and tools

CH_3OH, $HfCl_4$, NaOH, $AgNO_3$, and $HOC(COON_a)(CH_2COON_a)_2{\cdot}2H_2O$, which were used in the experimental synthesis of Ag, HfO_2, and Ag@HfO_2 core-shell nanoparticles synthesized within the scope of the study, were purchased from Chem. Lab. (Belgium), Alfa Easer (Germany), Isolab (Germany), and Merck (Germany), respectively. Rhodamine B (RhB), methylene blue (MB), and direct red-23 (DR-23) cationic dyes were bought from Sigma-Aldrich (China) for use in photocatalytic degradation studies. All chemicals were analytical purity and the water required for all solutions was obtained from Millipore Milli-Q Direct 16 ultrapure water systems. The properties of all chemicals have been shown in Table 1 and Table 2.

2.2. Synthesis of silver nanoparticles

Silver nitrate was used as a silver precursor to prepare Ag nanoparticles in a colloidal solution. Silver colloid was prepared using the chemical reduction method reported by Bastus et al. [19]. According to this method, a 100 mL aqueous solution containing tri-sodium citrate (TSC) (5 mM) was prepared and heated with a heating mantle under vigorous stirring for 15 min in a three-necked round bottom flask. Meanwhile, solvent evaporation was prevented utilizing a spiral refrigerant as shown in Fig. 1a. After boiling, 1 mL $AgNO_3$ (25 mM) was injected into this solution. Following the addition of $AgNO_3$, the color of the solution changed to bright yellow, indicating the formation of Ag nanoparticles (Fig. 1b). At this stage, it can be said that TSC functions as both a reducing and stabilizing agent as seen in Fig. 1c. Immediately after the synthesis of the Ag nuclei and in the same container, the reaction was cooled until the temperature of the solution reached 90 °C, and the solution was kept at this temperature for 15 min. The obtained solution was centrifuged at 10000 rpm, and Ag nanoparticles were separated from the solution. As a result, 12 mg Ag nanoparticles were obtained.

2.3. Synthesis of HfO_2 shell layers

For the synthesis of colloidal HfO_2 shell layers, the experimental procedure was followed previously used by Dhoke [21] to obtain ZnO nanoparticles. The synthesizing procedure schematically has been shown in Fig. 2. The decomposition of $HfCl_4$ salt in de-ionized water and its high solubility in methanol constrained the use of methanol as a solvent in the experimental process. For synthesis, a solution was obtained by mixing the appropriate amount of hafnium tetrachloride ($HfCl_4$) in a methanol solution at room temperature. In addition, analytical grade NaOH ($>$85 %) solution in 500 ml analytical grade methanol was prepared by cooling in an ice bath to obtain 0.1 M concentration of another solution. 100 mL of the second solution was then added very slowly and under vigorous stirring (1000 rpm/min) to the previously prepared solution, in which the $HfCl_4$ salt was completely dissolved until a white precipitate was observed. The white gel obtained after this step was mixed for about 3 h at a mixing speed of 1000 rpm/min, then it was washed 2 times in de-ionized water and centrifuged at 10000 rpm for 30 min. The obtained white powder was again dispersed in methanol and prepared for characteristic analysis.

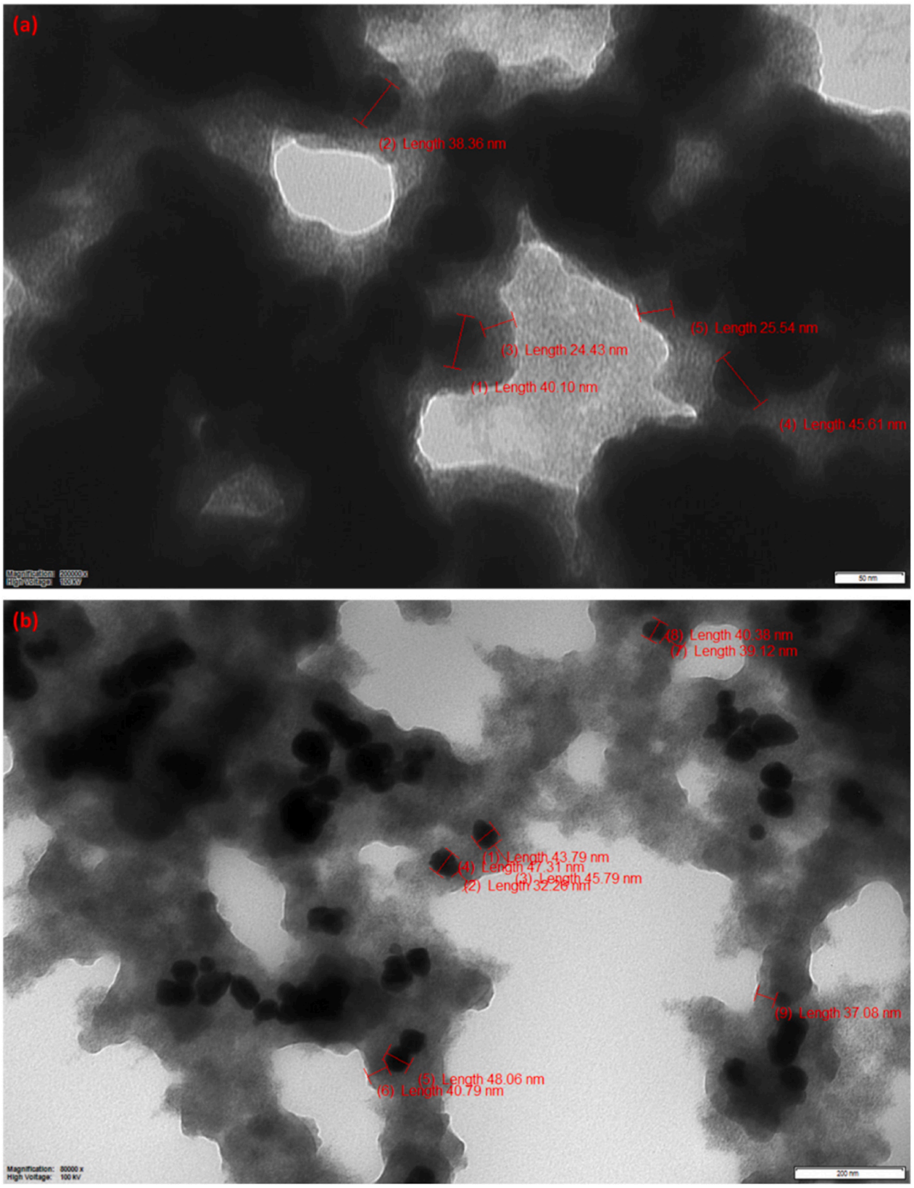

Fig. 5. Scaled representation of TEM images of a) Ag@HfO_2-1 and b) Ag@HfO_2-2 core-shell structures.

2.4. *Synthesis of Ag@HfO_2 core-shell nanoparticles*

6 mg of previously prepared Ag nanoparticles were divided into 3 different aliquots containing 40 mL methanol. 1.53 mL of $HfCl_4$ solution (Ag@HfO_2-1), which was prepared as 10 mM in methanol, to increase the thickness of the HfO_2 shell and, thus to cover the Ag nanoparticles with a strong dielectric material and to combine them with electromagnetic radiation of much larger wavelengths than these particles. To create a synergistic effect, 2.18 mL (Ag@HfO_2-2) and 2.80 mL (Ag@HfO_2-3) were added dropwise into aliquots containing Ag nanoparticles under vigorous stirring (1000 rpm/min) at room temperature very slowly. The resulting mixtures were stirred for 10 min at the same mixing speed and then added slowly in a controlled manner until a white precipitate was observed, indicating the formation of HfO_2, from the previously prepared 0.1 M NaOH solution. Since there was a possibility of oxidation of Ag nanoparticles by interacting with high NaOH, the NaOH addition process was carried out in a controlled and slow manner, as soon as a white precipitate (or discoloration) was observed. Then, NaOH addition was stopped, and this mixture was stirred at a mixing speed of 1000 rpm/min for 2 h. The resulting mixture was dispersed in 10 mL methanol after washing twice with water.

2.5. *Photo-catalytic performance measurements*

The photo-catalytic performance of Ag@HfO_2 core-shell nanoparticles was investigated considering the photodegradation of RhB, MB DR-23 dyes. Photo-catalytic activities of Ag@HfO_2 core-shell nanoparticles were carried out with an approach designed by Marien et al. [22]. For this, Ag@HfO_2 core-shell nanoparticles dispersed in methanol solvent were formed on 0.8 × 4 cm^2 glass substrate surfaces by drop casting method, and films containing approximately 1.5 mg Ag@HfO_2 catalyst were formed. These films were immersed in 3 ml of dye aqueous solutions containing 20 mM H_2O_2 (prepared to have a dye concentration of 5 mg/l) and exposed to a dark environment for 30 min. Since the dye content of the DR-23 cationic dye is 30 %, the dye concentration was prepared to be 25 mg/l in the photodegradation of the DR-23 dye, and thus the initial absorption was observed as ~0.99 %. The same way was followed for other dyes. Afterward, the solutions were illuminated using UV-A and visible region light sources with wavelengths of 350 nm and 420 nm. Photodegradation of the dyes was determined by using a

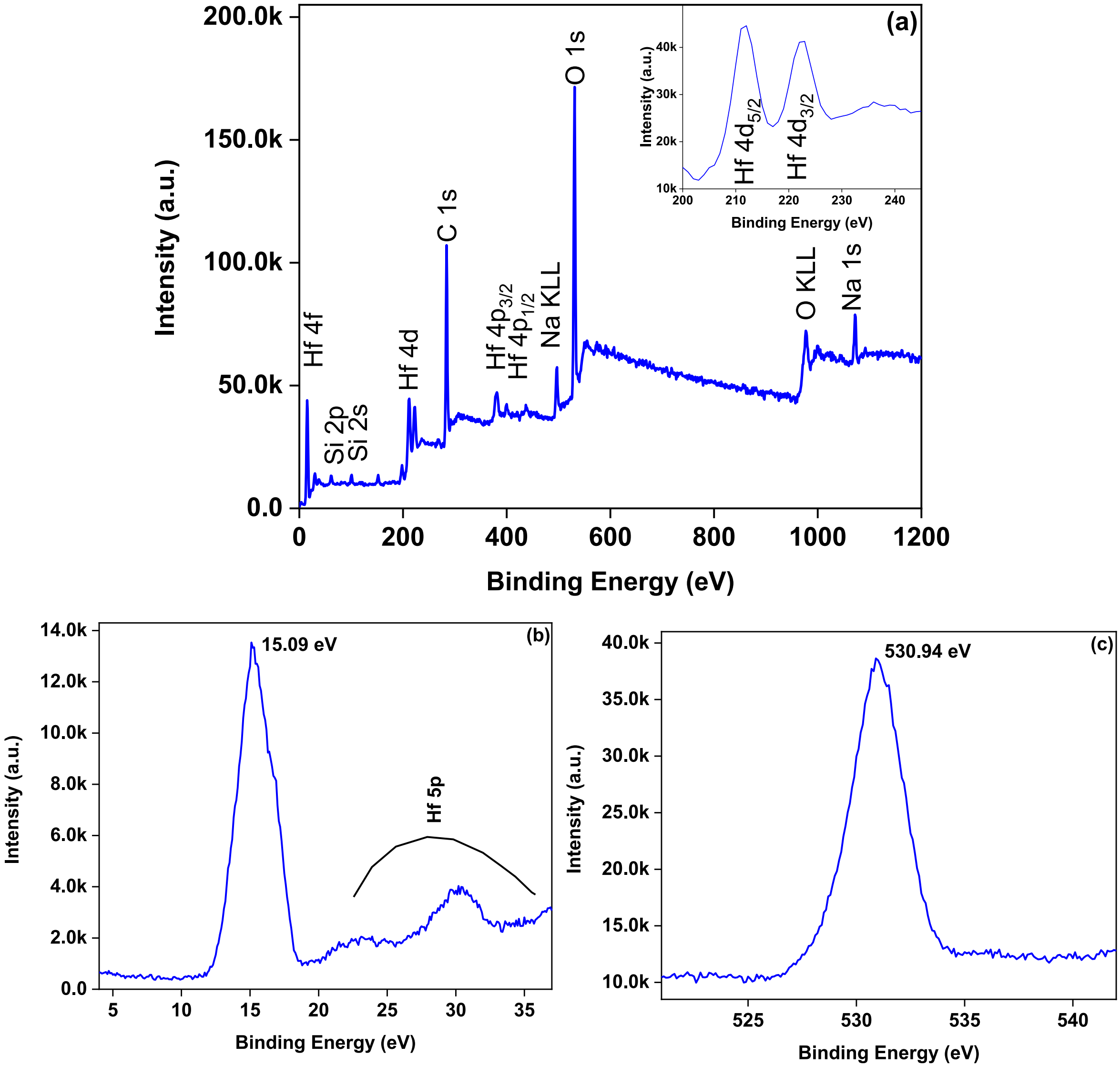

Figure 6. a) Overall scan for Ag@HfO_2-1 core-shell structures, XPS plots of b) Hf 4f and c) O 1s.

UV–Vis spectrometer and dye concentrations remaining at certain wavelenghts were determined at certain time intervals by using Beer-Lambert law.

2.6. *Characterization of synthesized structures*

PANalytical Empyrean brand X-ray diffractometer was used to characterize the crystalline structures of HfO_2, Ag, and Ag@HfO_2 nanostructures. JEOL JEM-1220 tunneling electron microscope was used to take images of the synthesized structures. Specs-Flex brand XPS device with 0.1° angular resolution was employed to obtain elemental compositions. MAPLE II- Low Temp Macro photoluminescence spectrometer and Shimadzu UV-3600 Plus brand UV-VIS-NIR spectrometer were used to obtain the optical properties of the nanostructures. Nyquist curves were performed in a three-electrode quartz cell using platinum (Pt) as the counter electrolyte, Ag/AgCl as the reference electrode, and HfO_2 and Ag@HfO_2 film-coated glassy carbon electrodes as the working electrode in 1 mM ferric/ferrous and 0.1 M KCl electrolyte solution. Measurements were obtained in the frequency range of 0.01–1 MHz under 10 mV AC potential.

3. Results and discussion

3.1. *Structural characterization*

XRD diffraction patterns of synthesized HfO_2, Ag, and Ag@HfO_2 nanostructures are shown in Fig. 3(a–d). From the diffraction pattern of HfO_2 shell layers in Fig. 3a, it is seen that these particles have a monoclinic polycrystalline structure, and the peaks of the pattern are quite compatible with the JCPDS 06-0318 card. The same XRD peaks of the HfO_2 shell layers or nanostructures can be seen in the literature [23–25]. These results revealed that desired HfO_2 shell layers were successfully synthesized. The XRD diffraction pattern of the synthesized Ag nanoparticles is seen in Fig. 3b. The peaks in Fig. 3b belonging to both Ag nanoparticles and Ag_2O are simultaneously located in the diffraction pattern as two separate phases. Such XRD patterns are available in the literature and can be attributed to the oxidation of Ag during production [26,27]. The Ag peaks reveal a face-centered cubic crystal structure and conform to the JCPDS 00-004-0783 card while the Ag_2O peak conforms to the JCPDS 00-019-1155 card. The results highlighted that Ag nanoparticles were successfully synthesized [28,29]. Normally, preferred orientation of the HfO_2 is generally ($\bar{1}$11) or (111) planes and (111) plane for Ag nanoparticles. However, the shapes of the nanoparticles as

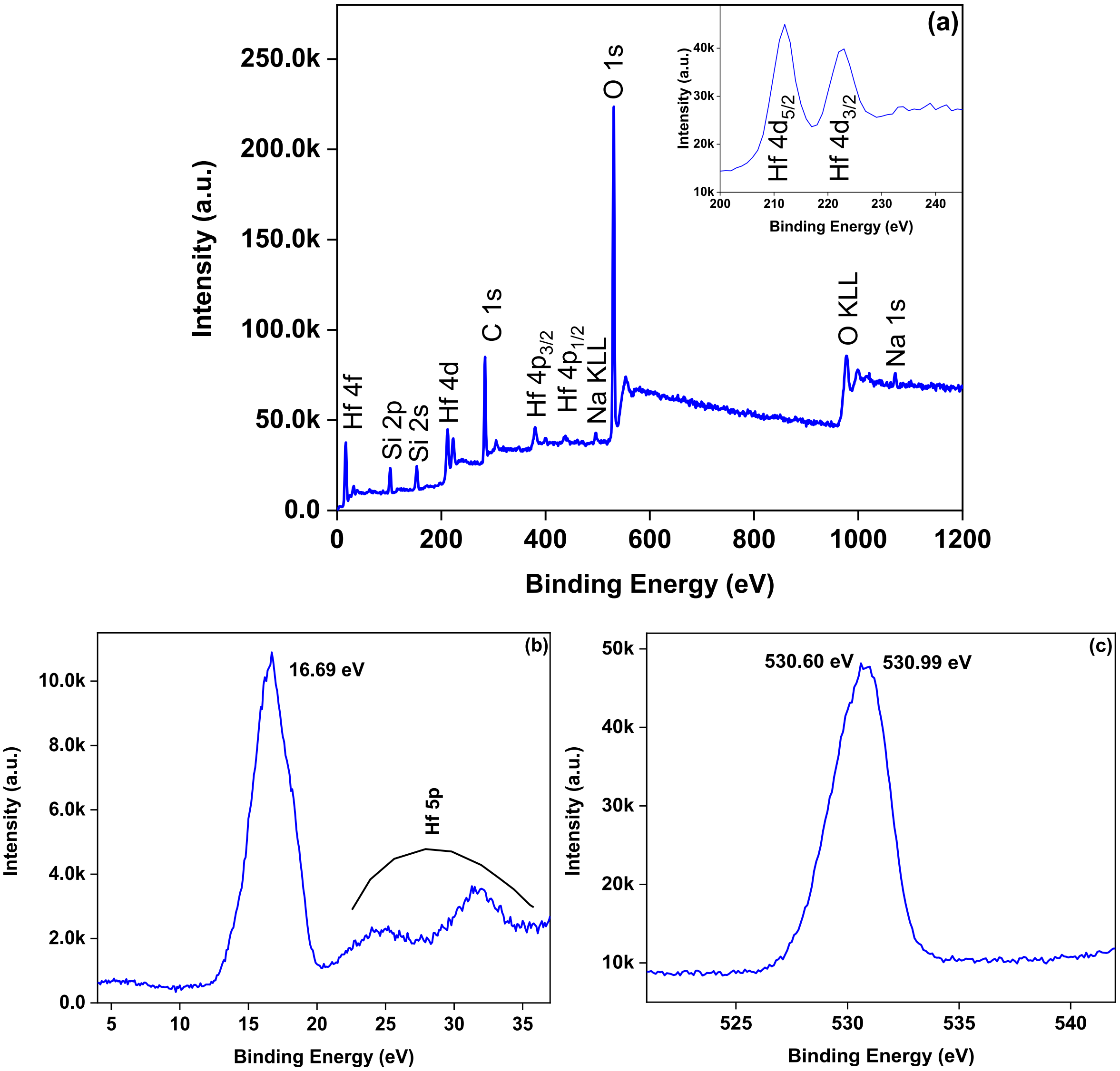

Fig. 7. a) Overall scan for Ag@HfO$_2$-2 core-shell structures, XPS plots of b) Hf 4f and c) O 1s.

well as agglomeration can change preferred orientation [30]. We think our XRD results have same results in the case of changing preferred orientation of synthesized nanoparticles.

XRD diffraction patterns of Ag@HfO$_2$-1 and Ag@HfO$_2$-2 core-shell structures are given in Fig. 3 (c) and (d), respectively. Here, the XRD pattern of HfO$_2$ shell layers almost overlaps with the XRD pattern of Ag nanoparticles, and it is difficult to distinguish them from each other. In Fig. 3 (c), although the degree values of the peaks are close to each other, the ($\bar{1}$11) and (111) peaks of HfO$_2$ are visible. However, other peaks are thought to overlap and belong to either Ag or HfO$_2$ shell layers [31]. In Fig. 3 (d), it is seen that the ($\bar{1}$11) and (111) peaks of HfO$_2$ have disappeared, but the other peaks in Fig. 3 (c) appear to belong to Ag and HfO$_2$.

TEM images of synthesized HfO$_2$, Ag, and Ag@HfO$_2$ nanostructures are displayed in Fig. 4(a–d). In Fig. 4a, it is seen from the TEM images of HfO$_2$ that the dimensions of the HfO$_2$ structures are at the nanometer level, but the particles are more agglomerated and these structures are dense in some places, but sparse in others. Although the TEM used does not have a selected area electron diffraction feature, it is thought that images very similar to the TEM images of HfO$_2$ are obtained in the literature [32]. This shows that HfO$_2$ shell layers were successfully synthesized. The TEM image of Ag nanoparticles is given in Fig. 4 (b), and Ag nanoparticles are around 30-50 nm dimensions with spherical and rod-like shapes which are quite similar to Ag nanostructures synthesized earlier in the literature [33,34].

In Fig. 4 (c) and 4 (d), approximately 30–40 nm core and 25-40 nm shell structures were obtained from the TEM images of Ag@HfO$_2$ core-shell nanostructures. With the increase in the density of HfO$_2$, a thickening of around 10-15 nm was detected in the shell. From these results, it was concluded that the Ag core structure can be successfully covered with the HfO$_2$ shell and its thickness can be controlled. In Fig. 5a and b, there are TEM images of Ag@HfO$_2$-1 and Ag@HfO$_2$-2 core-shell structures, respectively. The increase in shell thickness can be seen clearly as mentioned above with an increasing amount of HfCl$_4$ solution.

Fig. 6 and Fig. 7 show the overall scan, Hf 4f, and O 1s XPS spectra of Ag@HfO$_2$-1 and Ag@HfO$_2$-2 core-shell structures, respectively. In the general scan, Si 2p and Si 2s peaks of the glass substrate also appear in both spectra of Ag@HfO$_2$-1 and Ag@HfO$_2$-2 core-shell structures (Figs. 6a and 7a) [35]. In the general scan for both cases, the peaks of Hf 4d around 212 eV and 222 eV belonging to 4d5/2 and 4d3/2 peaks are given in the inset of Figs. 6a and 7a, C 1s peak around 281 eV, and Hf 4p peaks around 381 eV and 399 eV can be seen. Around 495 eV and 1072 eV, the Na (KLL) and Na 1s peaks caused by the impurities in the environment are located, respectively. Around 531 eV and 978 eV, there

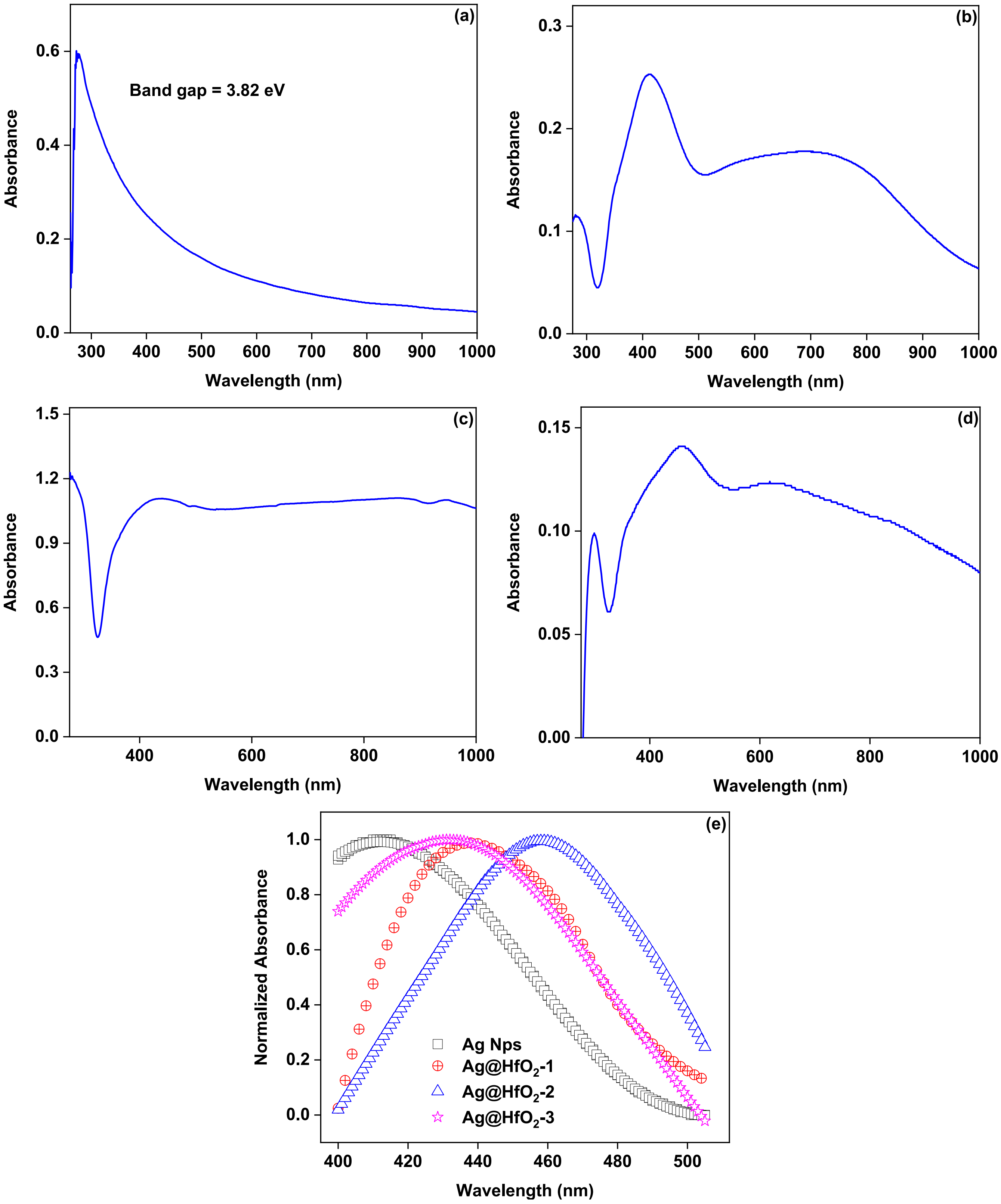

Fig. 8. Absorption spectra of a) HfO$_2$ shell layers, b) Ag nanoparticles, c) Ag@HfO$_2$-1, d) Ag@HfO$_2$-2 core-shell structures, and e) Shift in the normalized absorption band with HfO$_2$ shell thickness variation.

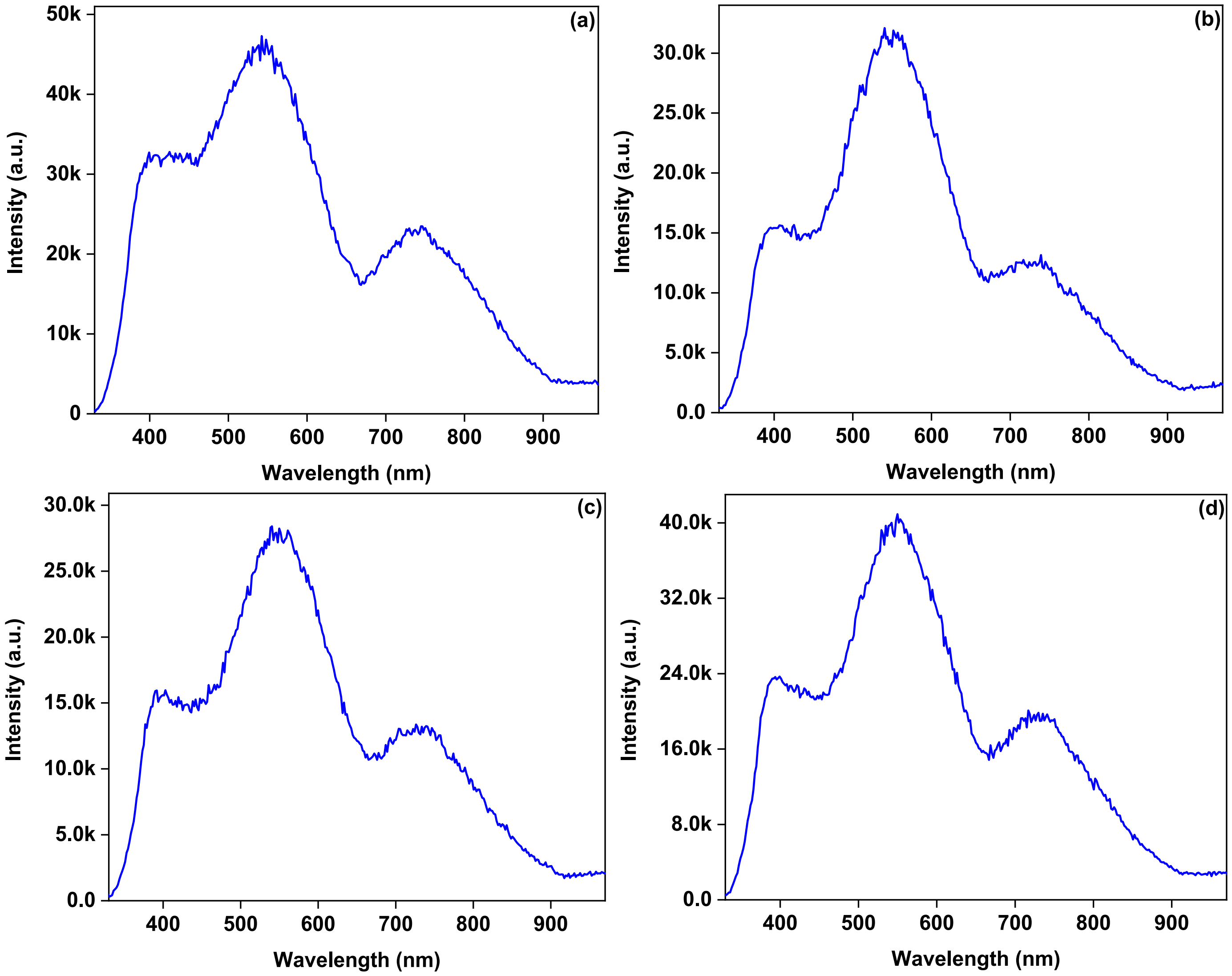

Figure 9. PL graphs of a) HfO_2 shell layers, b) Ag nanoparticles, c) Ag@HfO_2-1, and d) Ag@HfO_2-2 core-shell structures.

are O 1s and O (KLL) peaks, respectively. These peaks are the peaks of HfO_2 that could be seen in the literature [36–40]. High-resolution Hf 4f and O 1s peaks are given in Fig. 6b and c for the Ag@HfO_2-1 structure and in Fig. 7b and c for the Ag@HfO_2-2 structure. According to Fig. 6b and c, the Hf 4f and O 1s peaks appear as sharp peaks around 15.04 eV and 530.94 eV, respectively while in the case of the thicker HfO_2 shell, a cleavage is observed in the O 1s peak. The low-level peak can be attributed to oxygen defects, while the high-energy peak can be referred to surface hydroxides. The resulting XPS spectra show that HfO_2 structures were successfully obtained.

3.2. Optical characterization

Absorption graphs of synthesized HfO_2, Ag, and Ag@HfO_2 nanostructures obtained by UV–Vis spectrometer are given in Fig. 8a–e. According to the absorption graph for HfO_2 in Fig. 8a, it is seen that HfO_2 shell layers absorb more in the UV region and less in the visible region. The band gap energy of HfO_2 shell layers was determined as 3.82 eV by absorption spectrum. When the literature is examined, it has been determined that the 80 nm thin film structure of HfO_2 exhibits an absorption graph as obtained in Ref. [41]. It is understood from the TEM analysis results that the dimensions of the obtained HfO_2 nanostructures are around 50-60 nm. The absorption graph of Ag nanoparticles is given in Fig. 8b. An absorption peak around 410 nm and a broad peak around 690 nm are observed absorption graphs of Ag nanoparticles. The peak around 410 nm can be attributed to the surface plasmon frequency of Ag [42]. It can be said that Ag nanoparticles can have low absorption in a wide area from the UV region to the infrared (IR) region (0.20–0.25). Such low absorption values can be found in the literature [28]. The low absorption value here can be attributed to the agglomeration of nanoparticles [43,44]. Due to this agglomeration problem, it is thought that it would be appropriate to use Ag nanoparticles together with shells in photo-catalysis. The absorption spectrum of Ag@HfO_2 nanostructures with thin and thick shells (Ag@HfO_2 1-2) are given in Fig. 8c and d. While the absorption values of thin-shelled Ag@HfO_2 nanostructures cover both a high and wide range, the absorption values of thick-shell Ag@HfO_2 nanostructures decreased. Normalized absorption graphs obtained by adding silver nanoparticles and HfO_2 nanostructures for different shell thicknesses are given in Fig. 8e. The absorption graphs of the silver particles showed a red shift with the addition of a certain amount HfO_2 nanostructures, and after a certain rate, they shifted towards the blue region again. Therefore, the redshift of the SPR peak increases with increasing HfO_2 film thickness due to the increase in surface polarization energy. However, the SPR peak moves towards blue-shift as the HfO_2 film thickness increases further (for Ag@HfO_2-3), which can be attributed to the reduction of the surface polarization energy due to the diversity of the dielectric functions of Ag and HfO_2 [45]. This is the reason why the HfO_2 shell thickness cannot be increased

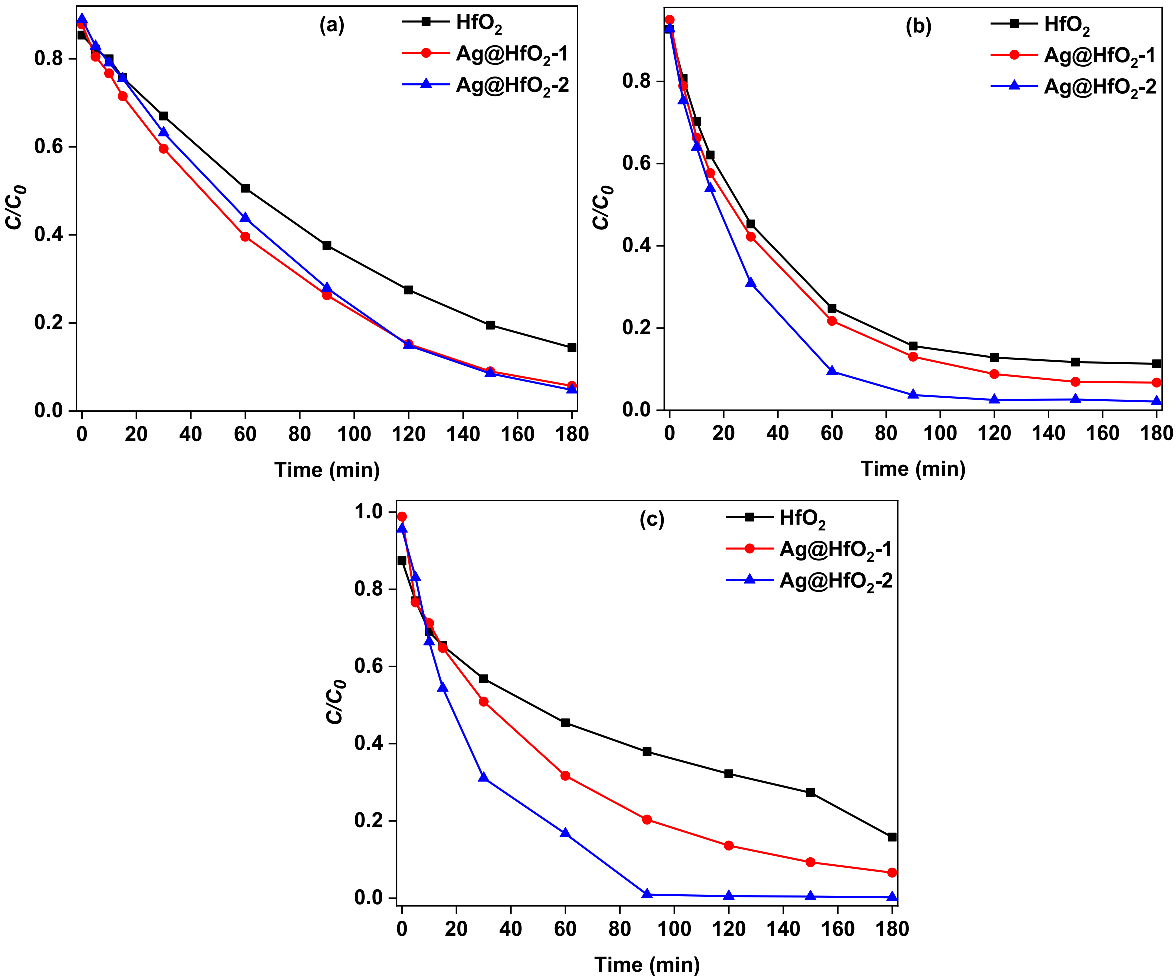

Fig. 10. Photodegradation curves of a) DR-23, b) MB, and c) RhB dyes by HfO_2 shell layers and different molarity Ag@HfO_2 core-shell structures in the UV-A region.

further in the framework of this study. Here, the desired absorption is shifted towards the red region and photodegradation takes place in the visible region. The results of Ag@HfO_2 structures shown in Fig. 8b and c are in agreement with the visible region photo-catalytic performances, and it has been confirmed that high-performance nanostructures are synthesized in the visible region.

The emission graphs of the synthesized HfO_2, Ag, and Ag@HfO_2 nanostructures obtained by PL spectrometry are given in Fig. 9(a)-9(d). A He-Cd laser with a wavelength of 325 nm was used to excite the samples, and the emission spectrums were obtained in the range of 200–1000 nm. According to the PL spectrum of HfO_2 in Fig. 9a, peaks around 420 nm, 544 nm, and 746 nm were observed. These three peaks in the spectrum can be attributed to oxygen defects, and such results are available in the literature [46–48]. The PL graph of Ag nanoparticles indicates again three peaks around 406 nm, 545 nm, and 740 nm according to Fig. 9b, and the PL peaks of Ag nanoparticles are quite similar to the peaks obtained in the literature [49]. The peaks here can be attributed to defects in the bonds formed with oxygen in the structure [50]. Wang et al. (2020) obtained dimensions of Ag nanoparticles around 40-50 nm, and the particles emitted narrow PL spectrum around 400 nm and wide PL spectrum in the range of 500–800 nm [51]. The spectrum of Ag nanoparticles creates a broad emission spectrum. Fig. 9 (c) and 9(d) show the PL emission spectrum of Ag@HfO_2-1 and Ag@HfO_2-2 core-shell structures. Overlapping peaks in these spectra were observed to sharpen with increasing HfO_2 shell thickness. It was concluded that the defect emission became more pronounced with increasing shell thickness.

3.3. *Photo-catalytic performance analysis*

The photo-catalytic performances of the obtained HfO_2 shell layers and Ag@HfO_2 core-shell structures were investigated considering the photodegradation of DR-23, MB, and RhB dyes for the UV-A region. UV-A region photo-catalytic performance curves of HfO_2 shell layers, Ag@HfO_2-1 and Ag@HfO_2-2 core-shell nanostructures of DR-23, MB, and RhB dyes are given in Fig. 10(a) and (b) and 10(c), respectively. As seen from the curves, Ag@HfO_2 core-shell structures are generally better for all three dyes than the photodegradation of HfO_2 shell layers. When the photo-catalytic performances of Ag@HfO2-2 core-shell structures are considered, it is seen that all dyes degraded within 180 min except DR-23 dye. According to some studies, HfO_2 shell layers do not completely degrade for MB dye, instead, HfO_2 shell layers are modified with graphene or Mn for good degradation [17,52]. It is important to note that the shell thicknesses of the core-shell materials should be adjusted for good photodegradation of the dyes. If the shell thickness is too large, localized holes can decrease photo-catalytic performance due to recombination of excitons in the core [53]. However, thick shell can provide higher local dielectric constant to provide red shift of the core. Rajbongshi et al. [54], studied Ag@ZnO core-shell structures for photodegradation of MB in the case of increasing shell thicknesses of ZnO from 6.76 nm to 40 nm, and they concluded that the increasing thickness caused more electron hole pairs, and more photoelectron transfer occurred from ZnO shell to Ag core. They also highlighted to that increasing ZnO shell provided to red shift from near UV to visible region for efficient solar light utilization. Shi et al. [55], investigated shell thickness effect of TiO_2@CdS core-shell structures for photodegradation

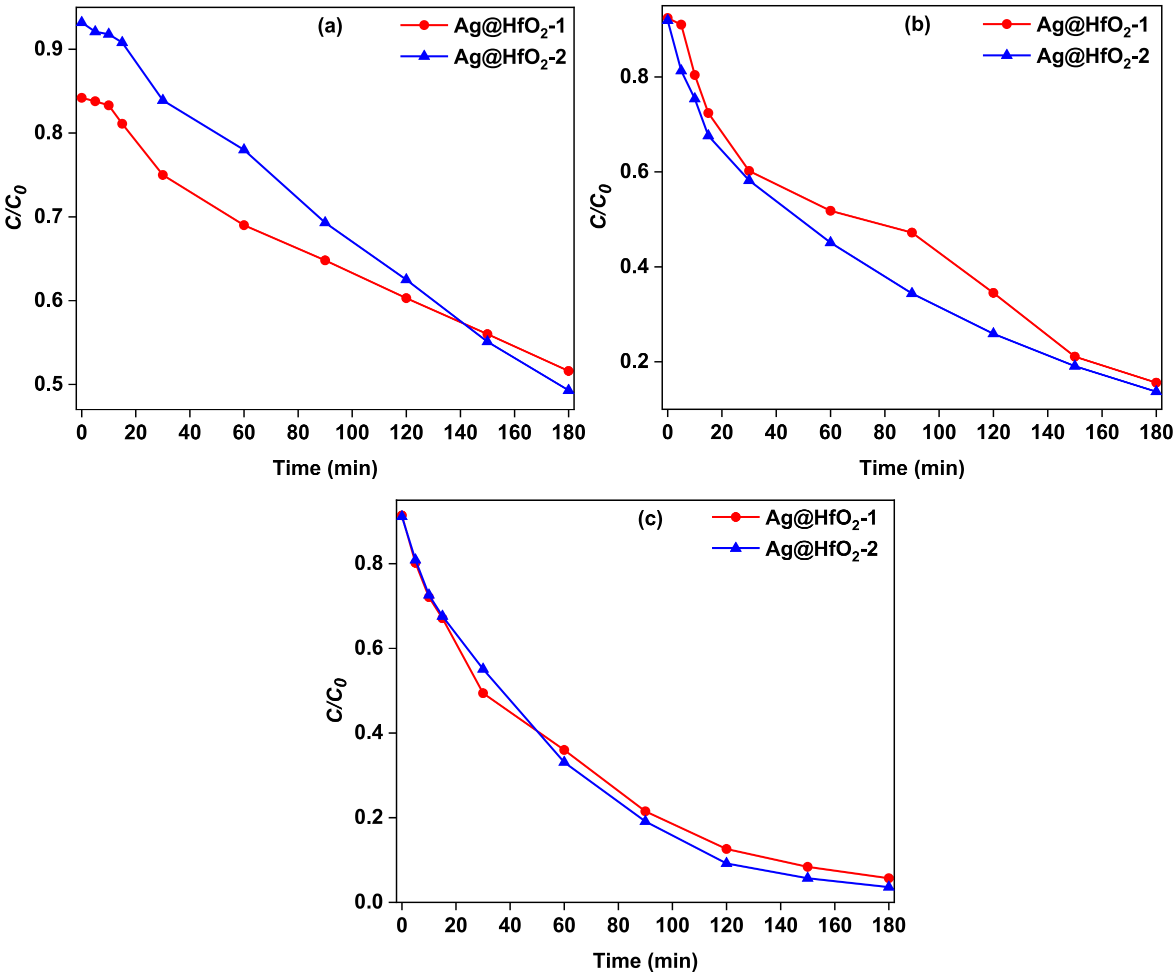

Figure 11. Photodegradation curves of a) DR-23, b) MB, and c) RhB dyes for different molarity ratios Ag@HfO_2 core-shell structures in the visible region.

Table 3
Degradation efficiencies, degradation rate, and correlation coefficients of synthesized structures for UV-A and visible region.

Situation	Structure	DR-23			MB			RhB		
		Efficiency (*η*)	*k* (min^{-1})	R^2	Efficiency (*η*)	*k* (min^{-1})	R^2	Efficiency (*η*)	*k* (min^{-1})	R^2
UV-A Region	HfO_2	% 83	0.00992	0.9991	% 88	0.01934	0.9547	% 82	0.00805	0.9842
	Ag@HfO_2-1	% 94	0.01511	0.9983	% 93	0.02102	0.9735	% 93	0.01463	0.9963
	Ag@HfO_2-2	% 95	0.01599	0.9949	% 98	0.03617	0.9542	% 99	0.03749	0.9753
Visible Region	HfO_2	–	–	–	–	–	–	–	–	–
	Ag@HfO_2-1	% 39	0.00275	0.9954	% 83	0.00915	0.9858	% 94	0.01564	0.9987
	Ag@HfO_2-2	% 47	0.00356	0.9985	% 85	0.00977	0.9975	% 96	0.01817	0.9987

of RhB dye, and they highlighted that the optimum thickness of CdS layer was 11 nm for better degradation. Li et al. [56], synthesized Ag@Cu_2O core-shell structures for photodegradation of methyl orange (MO) in visible region in the case of various shell thickness from 11 nm to 40 nm, and they reached that increasing shell thickness caused to increase local dielectric constant and provide red shift. Thus, entire visible region of light could be absorbed by Ag@Cu_2O core-shell structures and helped to increase photodegradation of MO. Lee et al. [57], also synthesized Ag@Cu_2O core-shell structures by simple co-reduction process to achieve various thicknesses of the Cu_2O shell (5.8 nm, 8.1 nm and 11 nm) for photodegradation of MO. They concluded that increasing shell thickness caused to red shift and increased photodegradation due to plasmonic charge transfer from the Ag core. Here, the thicknesses of the HfO_2 shells were adjusted by the amount of $HfCl_4$ solution to achieve various HfO_2 shells (samples called Ag@HfO_2-1, Ag@HfO_2-2 and Ag@HfO_2-3). According to TEM images of the Ag@HfO_2-1 and Ag@HfO_2-2, the samples have averagely ~25 nm and ~40 nm, respectively. Both of them caused to red shift according to absorption spectra (Fig. 8e). Thus, it is expecting better performance of the Ag@HfO_2-2 than Ag@HfO_2-1 core-shell.

In this study, core-shell structures were obtained with Ag nanoparticles and aimed to increase the photo-catalytic performance. It can be seen from the graphs that almost all of the MB and RhB dyes degrade within 90 min. It is seen that the results obtained are good enough compared to both the above-mentioned studies and other studies on HfO_2 [58]. The photo-catalytic performances of the obtained HfO_2 shell layers and Ag@HfO_2 core-shell structures were also discussed by photodegradation in the visible region for DR-23, MB, and RhB dyes. Visible region photo-catalytic performance curves of Ag@HfO_2-1 and Ag@HfO_2-2 core-shell structures for DR-23, MB, and RhB dyes are given in Fig. 11(a), (b), and (c), respectively. Here, the photodegradation curve of HfO_2 is not given since HfO_2 has wide band gap energy and

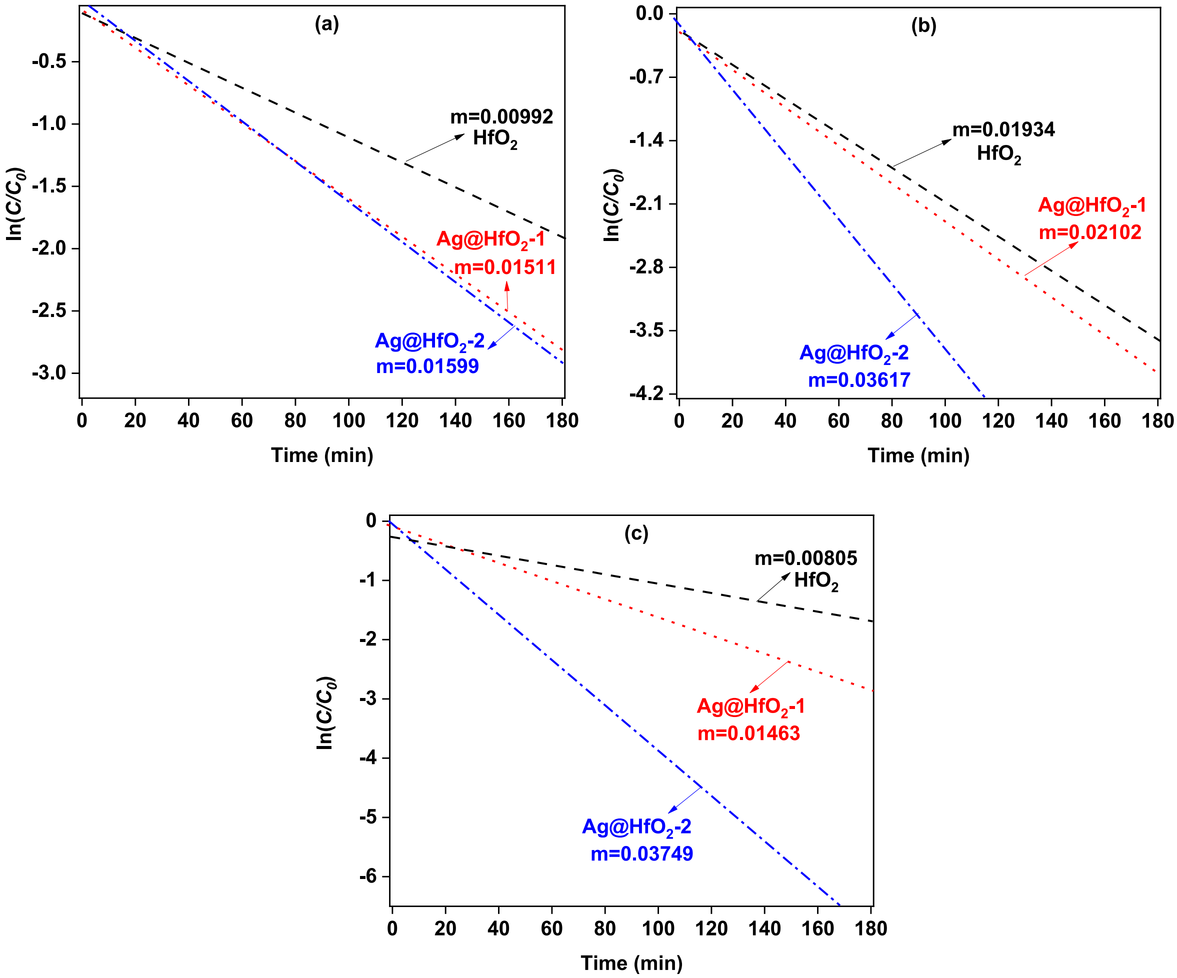

Fig. 12. Time variation of ln (C/C_0) values of a) DR-23, b) MB, and c) RhB dyes for different molarity ratios of Ag@HfO_2 in the UV-A region.

absorbs in the UV region [59]. When the degradation of DR-23, MB, and RhB dyes by Ag@HfO_2 core-shell structures is examined, it is seen that Ag@HfO_2-1 and Ag@HfO_2-2 core-shell structures affect the degradation of dyes. Although the degradation is not very good for DR-23, the degradation of MB and RhB dyes exhibit good result. Thus, it can be highlighted that Ag@HfO_2 core-shell structures can be successfully used in the degradation of MB and RhB dyes both in the visible region and in the UV-A region.

An important parameter used in the measurement of degradation is efficiency $\eta(\%)$. It is calculated by the following formula:

$$\eta(\%) = \frac{C_0 - C}{C_0} \times 100 \tag{1}$$

where C_0 represents the initial concentration value of the dye, and C represents the dye concentration value obtained after the degradation. By using this formula, the efficiency values of degradation with HfO_2 shell layers and Ag@HfO_2 core-shell structures for both the UV-A region and the visible region of DR-23, MB, and RhB dyes were calculated and given in Table 3.

While the degradation efficiency values of dyes with HfO_2 shell layers in the UV-A region were around 80 %, these values increased above 90 % for all dyes with Ag@HfO_2 core-shell structures. Moreover, with the increase in the density of the Ag@HfO_2 core-shell structures, the efficiency reached over 95 % for all three dye types. These results highlight that Ag@HfO_2 core-shell structures exhibit better efficiency in the UV-A region due to the plasmon frequency of Ag [42]. The photodegradation performance of Ag@HfO_2 core-shell structures were studied in the visible region, but HfO_2 shell layers were not studied due to not absorbing light in the visible region as shown in absorption graphs. Ag@HfO_2 core-shell structures also remove MR and RhB dyes with very good efficiency, except for DR-23 dye in the visible region. This may be attributed material reaction between HfO_2 and DR-23. Namely, energy absorption and transfer are affected by the number and position of chromophores in the dye molecules and the presence of auxochromes [60]. Since RhB and MB dyes have more efficient chromophores in their molecular structure than DR-23 dye, it is assumed in our study that there is less energy transfer to DR-23 dye by visible light, and consequently less degradation of DR-23 dye in the visible region. Furthermore, the degradation efficiency of Ag@HfO_2 core-shell structures increase with increasing concentration.

Another method used to evaluate photo-catalytic performance is to examine the kinetics of the catalytic reaction. The catalytic reaction kinetics is described by the following equation:

$$\ln(C/C_0) = -kt \tag{2}$$

where k represents the degradation rate coefficient, and t shows the reaction time. If ln (C/C_0) is plotted against time, the slope of this graph gives the coefficient of the degradation rate.

ln (C/C_0)– time graphs are displayed in Fig. 12 (a)-(c) for the UV-A region and Fig. 13(a–c) for the visible region. Here, instead of the fluctuation in the graphs, only the slopes are drawn to show the k-values. The k-values (with the corresponding correlation coefficients (R^2)) are given for HfO_2 shell layers and Ag@HfO_2 core-shell structures both in Table 3 and Figs. 12 and 13. According to ln (C/C_0)– time graphs and for

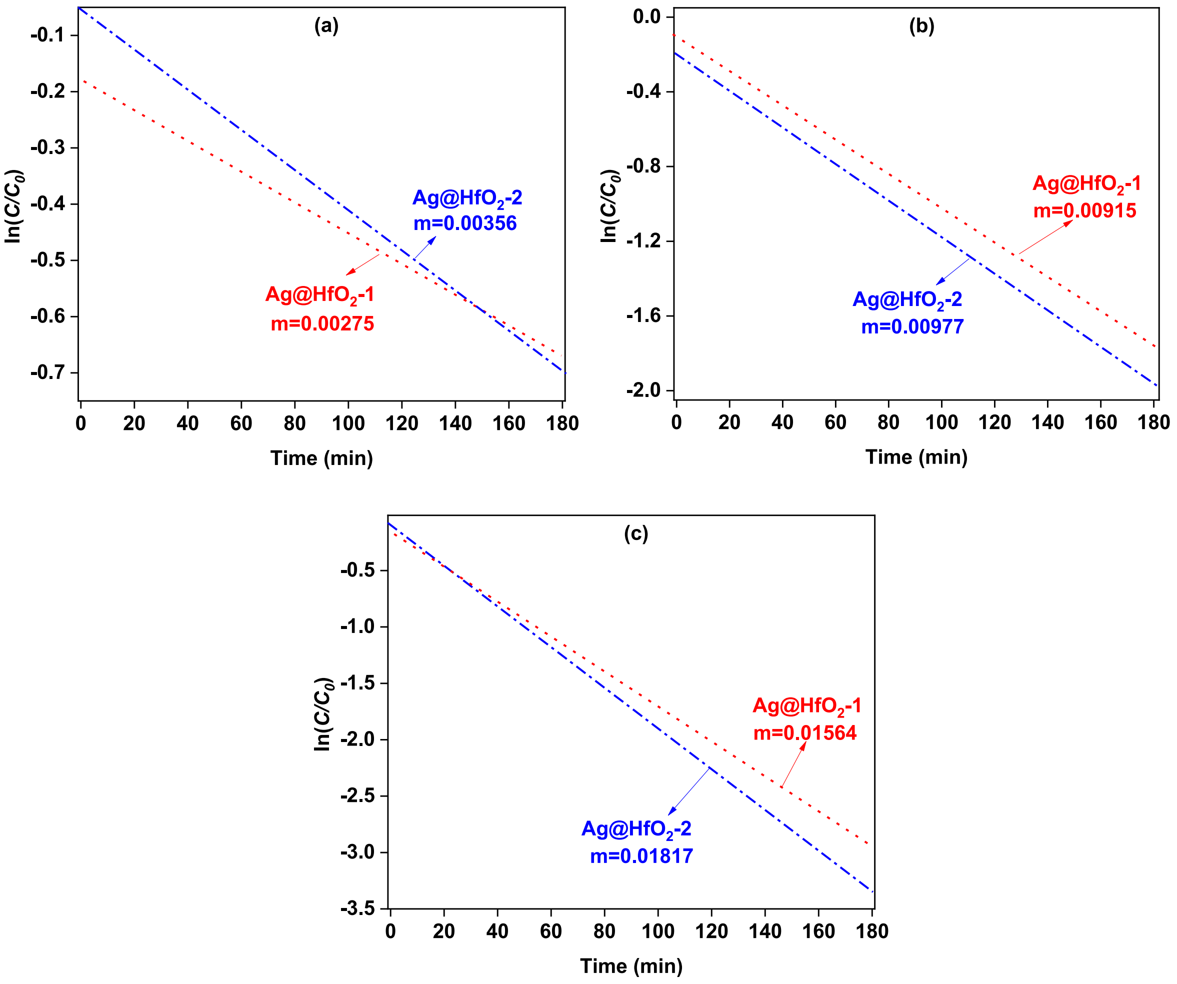

Fig. 13. Time variation of ln (C/C_0) values of a) DR-23, b) MB, and c) RhB dyes for different molarity ratios of Ag@HfO_2 in the visible region.

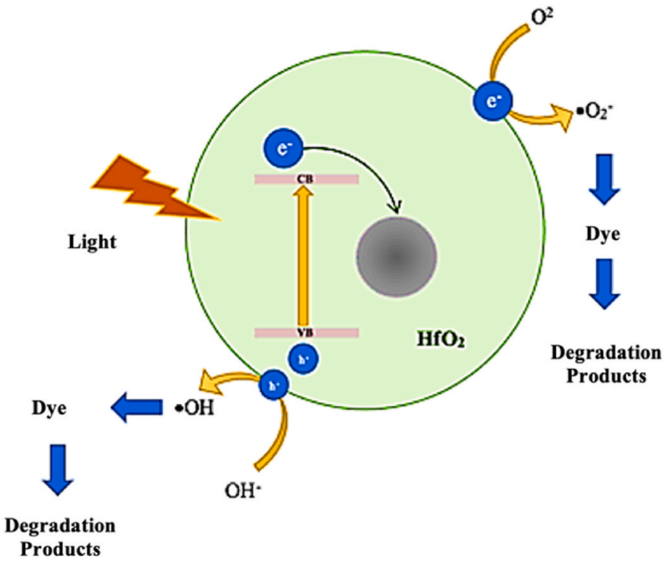

Fig. 14. Schematic view of the photo-catalytic mechanism of Ag@HfO_2 core-shell nanostructures under light.

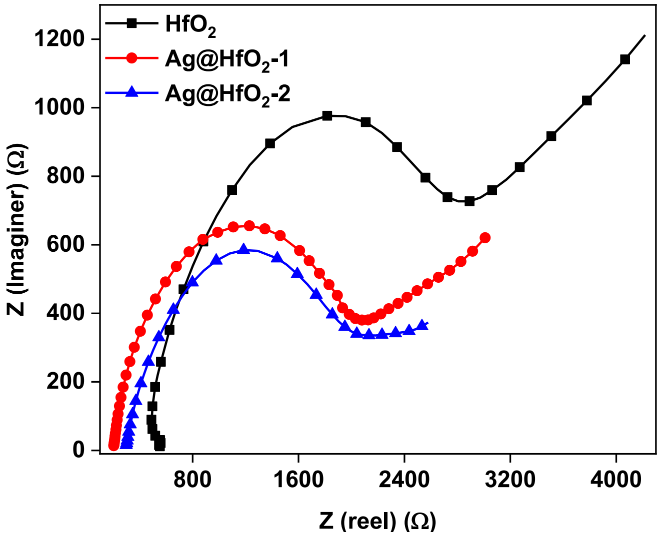

Fig. 15. Nyquist diagrams of synthesized HfO_2 and various concentrations of Ag@HfO_2 core-shell structures.

all three dyes, the slopes increased for both the UV-A region and the visible region by increasing molarity of Ag@HfO_2 core-shell structures. These results confirmed that increasing molarity of Ag@HfO_2 core-shell structures caused to increase degradation of the dyes, and Ag@HfO_2 core-shell exhibited better performance than HfO_2 shell layers. Moreover, all R^2 values were found to be above 0.95. This shows that time and the degradation rate coefficient are well correlated.

Table 4
Performance comparison of Ag@HfO_2 core-shell structures with previous literature.

Nanocomposites	Irradiation Source	Dye	Irradiation Time (min)	Degradation (%)	Refrences
Ag@HfO_2	UV–Visible	DR-23	180	95 (UV), 47 (Vis)	This work
Ag@HfO_2	UV–Visible	MB	180	98 (UV), 85 (Vis)	This work
Ag@HfO_2	UV–Visible	RhB	180	99 (UV), 96 (Vis)	This work
Ag@ZnO	Sunlight	MB	80	98	[54]
Ag@ZnO	Sunlight	MB	80	96	[42]
Au-Ag@TiO_2	Sunlight	MO	90	61	[66]
Ag@SnO_2	Visible light	RhB	90	88	[67]
Ag@Cu_2O	Visible light	MO	40	93	[68]

It is well known that the production of reactive radicals ($\bullet OH$, h$^+$ ve $\bullet O^{2-}$) is a crucial step for photo-catalysis [61]. Therefore, it is important to understand the nature of the reactive radicals responsible for photo-catalytic degradation. The photo-catalytic activity can be attributed to the formation of the Schottky barrier shown in Fig. 14 at the metal-semiconductor interface between the Ag core and the HfO_2 shell. Hence, it has been observed that photon-excited electrons cause rapid transfer from the high energy conduction band of the HfO_2 shell to the Ag core. As a result, prolonging the recombination times have caused increasing the photo-catalytic performance by forming electron-hole pairs.

Generated electrons on the surface of Ag nanoparticles by the surface plasmon resonance are transmitted with the HfO_2 shell and be trapped by the adsorbed O_2 molecules present in medium to produce superoxide anion radicals ($\cdot O_2^-$) [62]. Furthermore, the internal porosity within nanoparticles facilitates the diffusion of reactive oxygen species (ROS) originating from the formation of electron-hole pairs upon exposure to light into the HfO_2 layer. Concurrently, surface plasmon resonance (SPR) modifies the local electromagnetic field surrounding the nanoparticles, particularly in regions with restricted oxygen availability, potentially enhancing oxygen activation. These phenomena enable the proximity of Ag nanoparticles to facilitate contact with O_2 molecules. At the same time, it can be discussed that the holes formed in HfO_2 react with H_2O molecules adsorbed on the surface of the HfO_2 shell, resulting in $\bullet OH$ radicals. In such cases, the action of O^{2-} and $\bullet OH$ radicals may cause the dye molecules to decompose into CO_2 and H_2O products. Detailed explanation about photo-catalytic mechanism and possible reaction steps can be found in the literature for Ag plasmonic cores [42, 63]. The reactions of all the photo-catalytic processes mentioned above can be summarized as follows:

$$HfO_2 + h\nu \rightarrow HfO_2(e^-) + (h^+) \tag{3}$$

$$HfO_2(e^-) + Ag \rightarrow HfO_2 + Ag(e^-) \tag{4}$$

$$Ag(e^-) + O_2 \rightarrow \bullet O_2{}^- + Ag \tag{5}$$

$$HfO_2(h^+) + H_2O \rightarrow HfO_2 + \bullet OH + H^+ \tag{6}$$

$$\bullet O_2{}^- + \bullet OH + dye\ solution \rightarrow CO_2 + H_2O \tag{7}$$

The Nyquist plot obtained from electrochemical impedance spectroscopy (EIS) is a crucial method for studying the efficiency of interface charge separation. This efficiency is a key factor in determining the photo-catalytic activity of light-excited electrons and holes [64]. Fig. 15 shows Nyquist plots for HfO_2 shell layers, Ag@HfO_2-1, and Ag@HfO_2-2 core-shell structures. Since arc radius formations are seen in all three graphs, it can be said that interfacial layer resistance occurs on the electrode surface for all three structures [42]. While the arc radius is the largest for HfO_2 shell layers, the decrease in arc radius with increasing Ag@HfO_2 core-shell concentration indicates a better charge separation mechanism of the Ag@HfO_2 core-shell structure and rapid transfer of the separated charges to the electrodes [65]. It is seen that the obtained results are quite compatible with the photo-catalytic measurements.

Table 4 shows comparison of the degradation performance for Ag@HfO_2 core-shell structures depending on current literature for Ag core and metal oxide shells. Ag@HfO_2 core-shells exhibited good performance for three different dyes especially UV region. This performance might be improved to decrease aggregation of Ag@HfO_2 core-shells.

4. Conclusion

Ag@HfO_2 core-shell nanostructures were synthesized and the effectiveness of this catalyst was investigated to remove synthetic dyes or organic pollutants from drinking water. The suitability of the synthesized catalyst for removing the cationic dyes of rhodamine B, methylene blue, and direct red-23 pollutants from water was tested by photo-catalytic measurements. Characteristics of prepared core-shell nanostructures were evaluated by X-ray diffraction, transmission electron microscopy, X-ray photoelectron spectroscopy, UV-Vis and photoluminescence spectroscopy. The findings showed that Ag@HfO_2 core-shell nanostructures were well prepared and potentially a candidate catalyst for photodegradation. XRD patterns confirmed the crystal structures of the HfO_2 shell layers, Ag nanoparticles, and Ag@HfO_2 core-shell nanostructures. TEM micrographs showed that HfO_2 and Ag nanoparticles were about 30 to 50 nm, and Ag@HfO_2 core-shell nanostructures were in a successfully produced. XPS data showed that the HfO_2 shell layer was present in Ag@HfO_2 core-shell nanostructures with Hf 4d, Hf 4p and O 1s peaks. The results of UV-Vis and PL spectrometry have confirmed that the Ag@HfO_2 core-shell nanostructures both absorb and emit light in a broad spectrum ranging from the UV region to the visible region. Photo-catalytic studies showed that Ag@HfO_2 core-shell nanostructures can degrade corresponding dyes with high efficiency in both UV and visible region. It was observed that Ag@HfO_2 core-shell structures could serve as an alternative for degrading organic contaminants from drinking water.

Ethics approval

Not applicable.

Consent to participate

All the authors are consented to participate in the drafting of the paper.

Consent for publication

All authors are consented to publish the paper.

Funding

This study was supported by TUBITAK with grand number of 122F075.

CRediT authorship contribution statement

Adem Kocyigit: Data curation, Investigation, Writing – original draft. **Erman Erdogan:** Data curation, Investigation, Writing – original draft. **Nurtac Canpolat:** Investigation, Methodology. **Sakir Aydogan:** Investigation, Methodology. **Mehmet Yilmaz:** Data curation, Investigation, Methodology, Writing – review & editing.

Declaration of competing interest

The authors declare that they have no known competing financial interests or personal relationships that could have appeared to influence the work reported in this paper.

Data availability

Data will be made available on request.

Acknowledgments

This study was conducted as part of project number [122F075] entitled "Design of Ag@HfO_2 core-shell nanostructures with efficient sensitization mechanism for photocatalysis" supported by the Scientific and Technological Research Council of Turkey (TUBITAK). The authors would also like to thank Ibrahim Dagci for his contribution to this study.

References

[1] R. Djellabi, L. Noureen, V.D. Dao, D. Meroni, E. Falletta, D.D. Dionysiou, C. L. Bianchi, Recent advances and challenges of emerging solar-driven steam and the contribution of photocatalytic effect, Chem. Eng. J. 431 (2022) 134024, https://doi.org/10.1016/j.cej.2021.134024.

[2] H. Wang, X. Liu, Y. Wang, S. Zhang, G. Zhang, Y. Han, M. Li, L. Liu, Spatial and temporal dynamics of microbial community composition and factors influencing the surface water and sediments of urban rivers, J. Environ. Sci. (China). 124 (2023) 187–197, https://doi.org/10.1016/j.jes.2021.10.016.

[3] H. Ben Slama, A.C. Bouket, Z. Pourhassan, F.N. Alenezi, A. Silini, H. Cherif-Silini, T. Oszako, L. Luptakova, P. Golińska, L. Belbahri, Diversity of synthetic dyes from textile industries, discharge impacts and treatment methods, Appl. Sci. 11 (2021) 6255, https://doi.org/10.3390/app11146255.

[4] V. Karthik, P. Selvakumar, N. Sivarajasekar, P. Megavarshini, N. Brinda, J. Kiruthika, K. Balasubramani, T. Ahamad, M. Naushad, Comparative and Equilibrium studies on anionic and cationic dyes removal by nano-Alumina-doped Catechol Formaldehyde composite, J. Chem. 2020 (2020), https://doi.org/10.1155/2020/7617989.

[5] A. Singhal, A. Gupta, Efficient utilization of Sal deoiled seed cake (DOC) as reducing agent in synthesis of silver nanoparticles: Application in treatment of dye containing wastewater and harnessing reusability potential for cost-effectiveness, J. Mol. Liq. 268 (2018) 691–699, https://doi.org/10.1016/j.molliq.2018.07.092.

[6] K. Sharma, D. Vaya, G. Prasad, P.K. Surolia, Photocatalytic process for oily wastewater treatment: a review, Int. J. Environ. Sci. Technol. 20 (2023) 4615–4634, https://doi.org/10.1007/s13762-021-03874-2.

[7] M.R. Sohrabi, M. Ghavami, Photocatalytic degradation of Direct Red 23 dye using UV/TiO2: effect of operational parameters, J. Hazard Mater. 153 (2008) 1235–1239, https://doi.org/10.1016/j.jhazmat.2007.09.114.

[8] K. Nanaji, R.K. Siri Kiran Janardhana, T.N. Rao, S. Anandan, Energy level matching for efficient charge transfer in Ag doped - Ag modified TiO2 for enhanced visible light photocatalytic activity, J. Alloys Compd. 794 (2019) 662–671, https://doi.org/10.1016/j.jallcom.2019.04.283.

[9] C. Liu, Y. Qin, W. Guo, Y. Shi, Z. Wang, Y. Yu, L. Wu, Visible-light-driven photocatalysis over nano-TiO2 with different morphologies: from morphology through active site to photocatalytic performance, Appl. Surf. Sci. 580 (2022) 152262, https://doi.org/10.1016/j.apsusc.2021.152262.

[10] Y. Li, G. Hai, G. Ding, K. Wang, D. Zhang, Ag/TiO2/WO3 nanoparticles with efficient visible light photocatalytic activity, Optoelectron. Lett. 18 (2022) 1–5, https://doi.org/10.1007/s11801-022-1077-y.

[11] E. Alikhaidarova, D. Afanasyev, N. Ibrayev, N. Nuraje, Plasmonic enhanced polymer solar cell with inclusion of Ag@SiO2 core-shell nanostructures, Polym. Adv. Technol. 33 (2022) 1000–1008, https://doi.org/10.1002/pat.5574.

[12] M.S. Sajna, G. Vimal, K.K. Sadasivuni, Plasmonic Catalysis for energy conversion-an Overview and recent trends, Top. Catal. (2022) 1–20, https://doi.org/10.1007/s11244-021-01552-8.

[13] A. Sakthisabarimoorthi, S.A. Martin Britto Dhas, M. Jose, Nonlinear optical properties of Ag@SiO2 core-shell nanoparticles investigated by continuous wave He-Ne laser, Mater. Chem. Phys. 212 (2018) 224–229, https://doi.org/10.1016/J.MATCHEMPHYS.2018.03.047.

[14] Y. Zhang, F. Fu, Y. Li, D. Zhang, Y. Chen, One-step synthesis of Ag@TiO2 nanoparticles for enhanced photocatalytic performance, Nanomaterials 8 (2018) 1032, https://doi.org/10.3390/NANO8121032.

[15] J.E. Jaffe, R.A. Bachorz, M. Gutowski, Low-temperature polymorphs of ZrO2 and HfO2: a density-functional theory study, Phys. Rev. B - Condens. Matter Mater. Phys. 72 (2005) 144107, https://doi.org/10.1103/PhysRevB.72.144107.

[16] W. Ahmed, J. Iqbal, Mn doped ZrO2 nanoparticles: an optically tuned photocatalyst with superior structural, magnetic and dielectric characteristics, J. Phys. Chem. Solids. 160 (2022) 110285, https://doi.org/10.1016/J.JPCS.2021.110285.

[17] L.A. González, S. Gálvez-Barboza, E. Vento-Lujano, J.L. Rodríguez-Galicia, L. A. García-Cerda, Mn-modified HfO2 nanoparticles with enhanced photocatalytic activity, Ceram. Int. 46 (2020) 13466–13473, https://doi.org/10.1016/j.ceramint.2020.02.130.

[18] J. Pérez-Juste, I. Pastoriza-Santos, L.M. Liz-Marzán, P. Mulvaney, Gold nanorods: synthesis, characterization and applications, Coord. Chem. Rev. 249 (2005) 1870–1901, https://doi.org/10.1016/j.ccr.2005.01.030.

[19] N.G. Bastús, F. Merkoçi, J. Piella, V. Puntes, Synthesis of highly monodisperse citrate-stabilized silver nanoparticles of up to 200 nm: kinetic control and catalytic properties, Chem. Mater. 26 (2014) 2836–2846, https://doi.org/10.1021/cm500316k.

[20] V.V. Mokashi, A.H. Gore, V. Sudarsan, M.C. Rath, S.H. Han, S.R. Patil, G. B. Kolekar, Evaluation of interparticle interaction between colloidal Ag nanoparticles coated with trisodium citrate and safranine by using FRET: spectroscopic and mechanistic approach, J. Photochem. Photobiol. B Biol. 113 (2012) 63–69, https://doi.org/10.1016/j.jphotobiol.2012.05.006.

[21] S.K. Dhoke, Synthesis of nano-ZnO by chemical method and its characterization, Results Chem 5 (2023) 100771, https://doi.org/10.1016/j.rechem.2023.100771.

[22] C.B.D. Marien, T. Cottineau, D. Robert, P. Drogui, TiO2 Nanotube arrays: influence of tube length on the photocatalytic degradation of Paraquat, Appl. Catal. B Environ. 194 (2016) 1–6, https://doi.org/10.1016/J.APCATB.2016.04.040.

[23] N. Kumar, B.P.A. George, H. Abrahamse, V. Parashar, S.S. Ray, J.C. Ngila, A novel approach to low-temperature synthesis of cubic HfO2 nanostructures and their cytotoxicity, Sci. Rep. 7 (2017) 1–14, https://doi.org/10.1038/s41598-017-07753-0.

[24] A. Ramadoss, S.J. Kim, Synthesis and characterization of HfO2 nanoparticles by sonochemical approach, J. Alloys Compd. 544 (2012) 115–119, https://doi.org/10.1016/j.jallcom.2012.08.005.

[25] A. Ramadoss, K. Krishnamoorthy, S.J. Kim, Novel synthesis of hafnium oxide nanoparticles by precipitation method and its characterization, Mater. Res. Bull. 47 (2012) 2680–2684, https://doi.org/10.1016/j.materresbull.2012.05.051.

[26] O. Pawar, N. Deshpande, S. Dagade, S. Waghmode, P. Nigam Joshi, Green synthesis of silver nanoparticles from purple acid phosphatase apoenzyme isolated from a new source Limonia acidissima, J. Exp. Nanosci. 11 (2016) 28–37, https://doi.org/10.1080/17458080.2015.1025300.

[27] V.G. Pol, D.N. Srivastava, O. Palchik, V. Palchik, M.A. Slifkin, A.M. Weiss, A. Gedanken, Sonochemical deposition of silver nanoparticles on silica spheres, Langmuir 18 (2002) 3352–3357, https://doi.org/10.1021/LA0155552/ASSET/IMAGES/MEDIUM/LA0155552E00004.GIF.

[28] Y. Meng, A sustainable approach to fabricating ag nanoparticles/PVA hybrid nanofiber and its catalytic activity, Nanomaterials 5 (2015) 1124–1135, https://doi.org/10.3390/nano5021124.

[29] M. Sabzi, S. Mersagh Dezfuli, A study on the effect of compositing silver oxide nanoparticles by carbon on the electrochemical behavior and electronic properties of zinc-silver oxide batteries, Int. J. Appl. Ceram. Technol. 15 (2018) 1446–1458, https://doi.org/10.1111/ijac.13047.

[30] C.F. Holder, R.E. Schaak, Tutorial on powder X-ray diffraction for characterizing nanoscale materials, ACS Nano 13 (2019) 7359–7365, https://doi.org/10.1021/acsnano.9b05157.

[31] D. Munthala, A. Mangababu, S.V.S. Nageswara Rao, S. Pojprapai, A.P. Pathak, D. K. Avasthi, Swift heavy ion assisted growth of silver nanoparticles embedded in hafnium oxide matrix, J. Appl. Phys. 130 (2021), https://doi.org/10.1063/5.0054846.

[32] Y. Wan, X. Zhou, Formation mechanism of hafnium oxide nanoparticles by a hydrothermal route, RSC Adv. 7 (2017) 7763–7773, https://doi.org/10.1039/c6ra26663k.

[33] K. Sen Chou, K.C. Huang, H.H. Lee, Fabrication and sintering effect on the morphologies and conductivity of nano-Ag particle films by the spin coating method, Nanotechnology 16 (2005) 779–784, https://doi.org/10.1088/0957-4484/16/6/027.

[34] L. David, B. Moldovan, Green synthesis of biogenic silver nanoparticles for efficient catalytic removal of harmful organic dyes, Nanomaterials 10 (2020) 202, https://doi.org/10.3390/nano10020202.

[35] B. Guan, H. Siampour, Z. Fan, S. Wang, X.Y. Kong, A. Mesli, J. Zhang, Y. Dan, Nanoscale nitrogen doping in silicon by self-assembled monolayers, Sci. Rep. 5 (2015) 1–9, https://doi.org/10.1038/srep12641.

[36] I. Hoflijk, C. Zborowski, I. Vaesen, A. Vanleenhove, K. Artyushkova, T. Conard, High-energy x-ray photoelectron spectroscopy spectra of Al2O3 measured by Cr Kα, Surf. Sci. Spectra 29 (2022) 014021 https://doi.org/10.1116/6.0001577.

[37] P. Kondaiah, H. Shaik, G. Mohan Rao, Studies on RF magnetron sputtered HfO2 thin films for microelectronic applications, Electron, Mater. Lett. 11 (2015) 592–600, https://doi.org/10.1007/s13391-015-4490-6.

[38] S. Kumar, S. Kumar, S. Tiwari, S. Augustine, S. Srivastava, B.K. Yadav, B. D. Malhotra, Highly sensitive protein functionalized nanostructured hafnium oxide based biosensing platform for non-invasive oral cancer detection, Sensors Actuators, B Chem. 235 (2016) 1–10, https://doi.org/10.1016/j.snb.2016.05.047.

[39] X. Luo, Y. Li, H. Yang, Y. Liang, K. He, W. Sun, H.H. Lin, S. Yao, X. Lu, L. Wan, Z. Feng, Investigation of HfO2 thin films on Si by X-ray photoelectron spectroscopy, rutherford backscattering, grazing incidence X-ray diffraction and

Variable Angle Spectroscopic Ellipsometry, Crystals 8 (2018) 248, https://doi.org/10.3390/cryst8060248.

[40] J. Shi, A. Ravi, N.E. Richey, H. Gong, S.F. Bent, Molecular layer deposition of a hafnium-based hybrid thin film as an electron beam resist, ACS Appl. Mater. Interfaces 14 (2022) 27140–27148, https://doi.org/10.1021/acsami.2c04092.

[41] M. Ramzan, A.M. Rana, E. Ahmed, M.F. Wasiq, A.S. Bhatti, M. Hafeez, A. Ali, M. Y. Nadeem, Optical characterization of hafnium oxide thin films for heat mirrors, Mater. Sci. Semicond. Process. 32 (2015) 22–30, https://doi.org/10.1016/j.mssp.2014.12.079.

[42] H. Rajbongshi, S. Bhattacharjee, P. Datta, Photocatalytic activity of Ag/ZnO core-shell nanoparticles with shell thickness as controlling parameter under green environment, Mater. Res. Express 4 (2017) 025501, https://doi.org/10.1088/2053-1591/aa5cd3.

[43] A. Zhang, J. Zhang, Y. Fang, Photoluminescence from colloidal silver nanoparticles, J. Lumin. 128 (2008) 1635–1640, https://doi.org/10.1016/j.jlumin.2008.03.014.

[44] Z. Parang, A. Keshavarz, S. Farahi, S.M. Elahi, M. Ghoranneviss, S. Parhoodeh, Fluorescence emission spectra of silver and silver/cobalt nanoparticles, Sci. Iran. 19 (2012) 943–947, https://doi.org/10.1016/j.scient.2012.02.026.

[45] H. Zhou, C. Wang, Y. Lai, J. Yu, S. Cheng, Plasmon-enhanced upconversion luminescence of the composite films through tunable ZnO spacer, Appl. Phys. Mater. Sci. Process 127 (2021) 1–6, https://doi.org/10.1007/s00339-021-04462-4.

[46] R. Kumar, A. Vij, M. Singh, Defects assisted luminescence in m-HfO2 nanocrystals: an experimental and theoretical study, Optik 248 (2021) 168121, https://doi.org/10.1016/j.ijleo.2021.168121.

[47] J. Ni, Q. Zhou, Z. Li, Z. Zhang, Oxygen defect induced photoluminescence of Hf O2 thin films, Appl. Phys. Lett. 93 (2008), https://doi.org/10.1063/1.2952288.

[48] Y. Sebti, T. Chauveau, M. Chalal, Y. Lalatonne, C. Lefebvre, L. Motte, Assessment of the morphological, optical, and photoluminescence properties of HfO2Nanoparticles synthesized by a sol-gel method assisted by microwave irradiation, Inorg. Chem. 61 (2022) 6508–6518, https://doi.org/10.1021/acs.inorgchem.2c00277.

[49] P. Agarwal, V. Kumar, S. Kachhwaha, S. Kothari, Green synthesis of silver nanoparticles using callus extract of capsicum annuum L. And their activity against microorganisms, Int. J. Nanotechnol. Appl. 4 (2014) 1–8. http://www.tjprc.org/view_paper.php?id=4087. (Accessed 10 July 2023).

[50] K. Kayed, The luminescence properties of individual silver nanoparticles in Ag/Ag2O composites synthesized by oxygen plasma treatment of silver thin films, J. Lumin. 237 (2021) 118163, https://doi.org/10.1016/J.JLUMIN.2021.118163.

[51] H.C. Wang, Y. Hong, Z. Chen, C. Lao, Y. Lu, Z. Yang, Y. Zhu, X. Liu, ZnO UV photodetectors modified by Ag nanoparticles using all-inkjet-printing, Nanoscale Res. Lett. 15 (2020) 1–8, https://doi.org/10.1186/s11671-020-03405-x.

[52] V. Jayaraman, S. Mahalingam, S. Chinnathambi, G.N. Pandian, A. Prakasarao, S. Ganesan, J. Ramasamy, S. Ayyaru, Y.H. Ahn, Facile synthesis of hafnium oxide nanoparticle decorated on graphene nanosheet and its photocatalytic degradation of organic pollutants under UV-light irradiation, Appl. Sci. 12 (2022) 11222, https://doi.org/10.3390/app122111222.

[53] H. Zhao, L. Qian, H. Lv, Y. Wang, G. Zhao, Introduction of a Fe3O4 core enhances the photocatalytic activity of MIL-100(Fe) with tunable shell thickness in the presence of H2O2, ChemCatChem 7 (2015) 4148–4155, https://doi.org/10.1002/cctc.201500801.

[54] H. Rajbongshi, S. Bhattacharjee, P. Datta, Shell thickness dependent photocatalytic activity of EDTA-assisted Ag/ZnO core-shell nanoparticles under sunlight irradiation, Mater. Res. Express 6 (2019) 045022, https://doi.org/10.1088/2053-1591/aafadd.

[55] Z. Shi, J. Liu, H. Lan, X. Li, B. Zhu, J. Yang, Effect of CdS shell thickness on the photocatalytic properties of TiO2@CdS core–shell nanorod arrays, J. Mater. Sci. Mater. Electron. 30 (2019) 17682–17692, https://doi.org/10.1007/s10854-019-02118-x.

[56] J. Li, S.K. Cushing, J. Bright, F. Meng, T.R. Senty, P. Zheng, A.D. Bristow, N. Wu, Ag@Cu2O core-shell nanoparticles as visible-light plasmonic photocatalysts, ACS Catal. 3 (2013) 47–51, https://doi.org/10.1021/cs300672f.

[57] C. Lee, K. Shin, Y.J. Lee, C. Jung, H.M. Lee, Effects of shell thickness on Ag-Cu2O core-shell nanoparticles with bumpy structures for enhancing photocatalytic activity and stability, Catal. Today 303 (2018) 313–319, https://doi.org/10.1016/j.cattod.2017.08.016.

[58] F.N.I. Sari, S.H. Lu, J.M. Ting, Wide-bandgap HfO2-V2O5 nanowires heterostructure for visible light-driven photocatalytic degradation, J. Am. Ceram. Soc. 103 (2020) 2252–2261, https://doi.org/10.1111/jace.16870.

[59] M.C. Cheynet, S. Pokrant, F.D. Tichelaar, J.L. Rouvìre, Crystal structure and band gap determination of Hf O2 thin films, J. Appl. Phys. 101 (2007), https://doi.org/10.1063/1.2697551.

[60] W.-K. Jo, R.J. Tayade, Recent developments in photocatalytic dye degradation upon irradiation with energy-efficient light emitting diodes, Chinese J. Catal. 35 (2014) 1781–1792, https://doi.org/10.1016/S1872-2067(14)60205-9.

[61] H. Jiang, X. Meng, Photocatalytic oxygen reduction, in: Photo- Electro-Catalytic Process, Wiley, 2022, pp. 389–413, https://doi.org/10.1002/9783527830084.ch12.

[62] M. Anpo, M. Che, B. Fubini, E. Garrone, E. Giamello, M.C. Paganini, Generation of superoxide ions at oxide surfaces, Top. Catal. 8 (1999) 189–198, https://doi.org/10.1023/a:1019117328935.

[63] A.N. Kadam, D.P. Bhopate, V.V. Kondalkar, S.M. Majhi, C.D. Bathula, A.-V. Tran, S.-W. Lee, Facile synthesis of Ag-ZnO core–shell nanostructures with enhanced photocatalytic activity, J. Ind. Eng. Chem. 61 (2018) 78–86, https://doi.org/10.1016/j.jiec.2017.12.003.

[64] W. Tu, Y. Zhou, Z. Zou, Versatile graphene-promoting photocatalytic performance of semiconductors: basic principles, synthesis, solar energy conversion, and environmental applications, Adv. Funct. Mater. 23 (2013) 4996–5008, https://doi.org/10.1002/adfm.201203547.

[65] D. Li, F. Shi, D. Jiang, M. Chen, W. Shi, CdIn2S4/g-C3N4 heterojunction photocatalysts: enhanced photocatalytic performance and charge transfer mechanism, RSC Adv. 7 (2017) 231–237, https://doi.org/10.1039/c6ra24809h.

[66] X. Yang, J. Liang, H. Fu, X. Ran, X. An, Fabrication of Au-Ag@TiO2 ternary core-shell nanostructures with enhanced sunlight photocatalytic activity, Powder Technol. 404 (2022) 117463, https://doi.org/10.1016/j.powtec.2022.117463.

[67] A. Baranowska-Korczyc, E. Mackiewicz, K. Ranoszek-Soliwoda, J. Grobelny, G. Celichowski, Core/shell Ag/SnO2 nanowires for visible light photocatalysis, Catalysts 12 (2021) 30, https://doi.org/10.3390/catal12010030.

[68] S. Tao, M. Yang, H. Chen, M. Ren, G. Chen, Microfluidic synthesis of Ag@Cu2O core-shell nanoparticles with enhanced photocatalytic activity, J. Colloid Interface Sci. 486 (2017) 16–26, https://doi.org/10.1016/j.jcis.2016.09.051.